RESEARCH ARTICLE

Orthogonal topography in the parallel input architecture of songbird HVC

Kevin C. Elliott[1] | Wei Wu[2] | Richard Bertram[3] | Richard L. Hyson[1] | Frank Johnson[1]

[1]Program in Neuroscience and Department of Psychology, Florida State University, Tallahassee, Florida

[2]Program in Neuroscience and Department of Statistics, Florida State University, Tallahassee, Florida

[3]Program in Neuroscience and Department of Mathematics, Florida State University, Tallahassee, Florida

Correspondence
Frank Johnson, Program in Neuroscience and Department of Psychology, Florida State University, Tallahassee, FL 32306-4301.
Email: johnson@psy.fsu.edu

Funding information
This work was supported by the National Science Foundation (IOS-1146607; IOS-1456965).

Abstract

Neural activity within the cortical premotor nucleus HVC (acronym is name) encodes the learned songs of adult male zebra finches (*Taeniopygia guttata*). HVC activity is driven and/or modulated by a group of five afferent nuclei (the Medial Magnocellular nucleus of the Anterior Nidopallium, MMAN; Nucleus Interface, Nif; nucleus Avalanche, Av; the Robust nucleus of the Arcopallium, RA; the Uvaeform nucleus, Uva). While earlier evidence suggested that HVC receives a uniformly distributed and nontopographic pattern of afferent input, recent evidence suggests this view is incorrect (Basista et al., 2014). Here, we used a double-labeling strategy (varying both the distance between and the axial orientation of dual tracer injections into HVC) to reveal a massively parallel and in some cases topographic pattern of afferent input. Afferent neurons target only one rostral or caudal location within medial or lateral HVC, and each HVC location receives convergent input from each afferent nucleus in parallel. Quantifying the distributions of single-labeled cells revealed an orthogonal topography in the organization of afferent input from MMAN and Nif, two cortical nuclei necessary for song learning. MMAN input is organized across the lateral-medial axis whereas Nif input is organized across the rostral-caudal axis. To the extent that HVC activity is influenced by afferent input during the learning, perception, or production of song, functional models of HVC activity may need revision to account for the parallel input architecture of HVC, along with the orthogonal input topography of MMAN and Nif.

KEYWORDS
premotor cortex, vocal learning, zebra finch, RRID: SCR_001775, RRID: SCR_014199, RRID: SCR_001622

1 | INTRODUCTION

The learned songs of adult male zebra finches are encoded within HVC, a premotor region of avian cortex. Numerous studies using a variety of experimental manipulations to target HVC—ablative, electrophysiological, pharmacological, thermal, and optogenetic—have shown remarkably specific effects on the learning and/or production of song (Andalman, Foerster, & Fee, 2011; Aronov, Andalman, & Fee, 2008; Aronov, Veit, Goldberg, & Fee, 2011; Basista et al., 2014; Hamaguchi & Mooney, 2012; Long & Fee, 2008; Nottebohm, Stokes, & Leonard, 1976; Poole, Markowitz, & Gardner, 2012; Roberts, Gobes, Murugan, Ölveczky, & Mooney, 2012; Scharff, Kirn, Grossman, Macklis, & Nottebohm, 2000; Simpson & Vicario, 1990; Stauffer et al., 2012; Thompson & Johnson, 2007; Thompson, Wu, Bertram, & Johnson, 2007; Williams, Crane, Hale, Esposito, & Nottebohm, 1992; Vu, Mazurek, & Kuo, 1994). Moreover, HVC neural activity is tightly correlated with the learning and production of song (Amador, Perl, Mindlin, & Margoliash, 2013; Jarvis & Nottebohm, 1997; Jarvis, Scharff, Grossman, Ramos, & Nottebohm, 1998; Jin & Clayton, 1997; Hahnloser, Kozhevnikov, & Fee, 2002; Hamaguchi, Tschida, Yoon, Donald, & Mooney, 2014; Kosche, Vallentin, & Long, 2015; Kozhevnikov & Fee, 2007; Long & Fee, 2008; Long, Jin, & Fee, 2010; Lynch, Okubo, Hanuschkin, Hahnloser, & Fee, 2016; Markowitz et al., 2015; Okubo, Mackevicius, Payne, Lynch, & Fee, 2015; Picardo et al., 2016; Vallentin & Long, 2015; Yu & Margoliash, 1996). Given this abundance of evidence, which clearly demonstrates the importance of
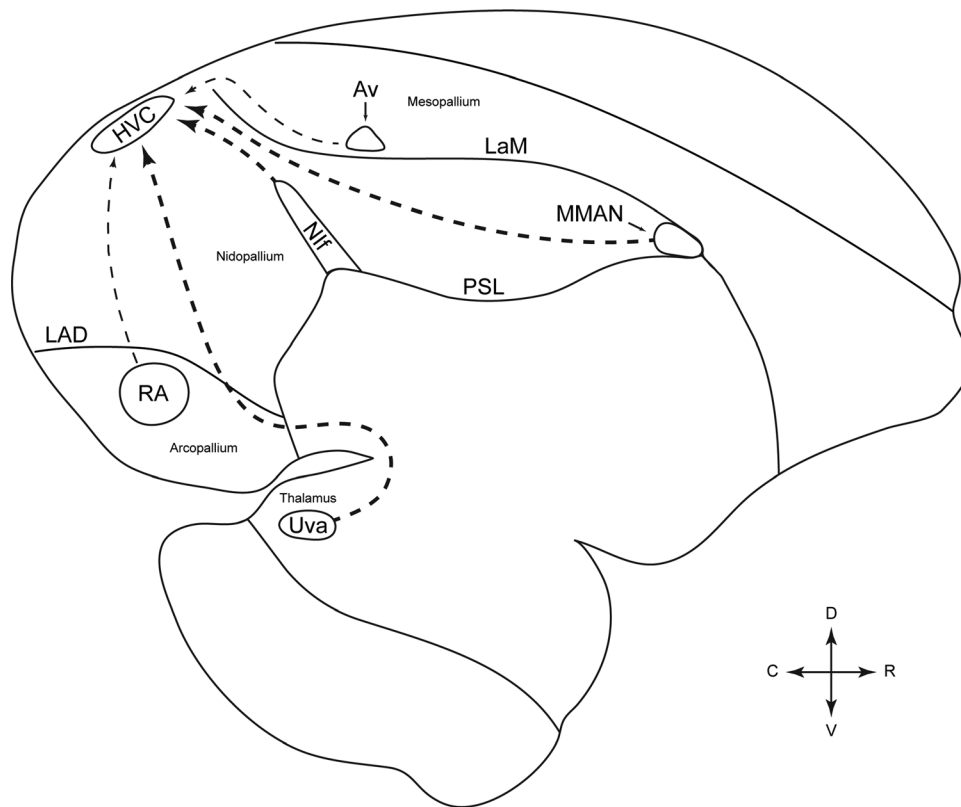
FIGURE 1 Sagittal schematic of HVC afferent input nuclei in an adult male zebra finch brain. HVC, a vocal premotor region located at the dorsal surface of the caudal telencephalon, receives afferent input from one thalamic nucleus (Uva) and four cortical nuclei (MMAN, NIf, Av, RA). The smaller dashed lines from Av and RA to HVC represent the smaller populations of labeled cells observed in these nuclei. Note that Uva also sends afferent projections to NIf and Av, and that NIf and Av are reciprocally connected (Akutagawa & Konishi, 2010). Av = Nucleus Avalanche; HVC = acronym is proper name; LAD = Dorsal Arcopallial Lamina; LaM = Mesopallial lamina; MMAN = Medial Magnocellular nucleus of the Anterior Nidopallium; NIf = Nucleus Interface; PSL = Pallial-Subpallial Lamina; RA = Robust Nucleus of the Arcopallium; Uva = Uvaeform nucleus

HVC for the learning and production of song, surprisingly little is known about the pattern of afferent input connectivity that drives and/or modulates HVC neural activity.

Until recently all tract-tracing evidence from adult birds indicated a uniformly distributed, nontopographic pattern of input from each of HVC's five afferent nuclei (MMAN, NIf, Uva, Av, RA, see Figure 1). The absence of topography was interpreted as evidence of a pattern of convergent afferent input, with widely branched axon terminals from each afferent nucleus overlapping one another with no specific pattern throughout the volume of HVC (Akutagawa & Konishi, 2010; Bauer et al., 2008; Bottjer, Halsema, Brown, & Miesner, 1989; Foster & Bottjer, 1998; Fortune & Margoliash, 1995; Nottebohm, Kelley, & Paton, 1982; Roberts, Klein, Kubke, Wild, & Mooney, 2008). However, using a new surgical approach to target HVC and paired injections of two different tracers, we have found that afferent projections onto medial and lateral HVC are in fact organized in parallel, where distinct subpopulations of cells within each HVC afferent nucleus project exclusively to medial or lateral HVC (Basista et al., 2014). This parallel input architecture complements recent evidence that adult HVC neurons are interconnected primarily along the rostral-caudal axis (Day, Terleski, Nykamp, & Nick, 2013; Nottebohm et al., 1982; Stauffer et al., 2012) and that medial and

lateral HVC can function independently in the production of adult song (Basista et al., 2014; Poole et al., 2012).

Here, we varied both the distance between and the axial orientation of paired tracer injections into HVC to further characterize the input architecture of HVC in adult birds. Like paired tracer injections into medial and lateral HVC (Basista et al., 2014), we find distinct single-labeled subpopulations of cells within all HVC afferent nuclei when paired tracer injections target rostral and caudal HVC. The overall pattern of labeling suggests that the terminals from each afferent neuron address only one rostral or caudal location within medial or lateral HVC, and that each HVC location receives convergent input from each afferent nucleus in parallel. Moreover, although the pattern of retrograde labeling within each afferent nucleus lacks consistent point-to-point topography, by quantifying the distribution density of labeled cells we document a population-level orthogonal topography in two of HVC's afferent nuclei, MMAN and NIf. MMAN input is organized topographically across the lateral-medial axis of HVC whereas NIf input is organized topographically across the rostral-caudal axis of HVC, albeit inversely. Our results reveal a massively parallel input architecture for HVC that features orthogonal topography across the two major axes of HVC. This newly defined input architecture may have useful
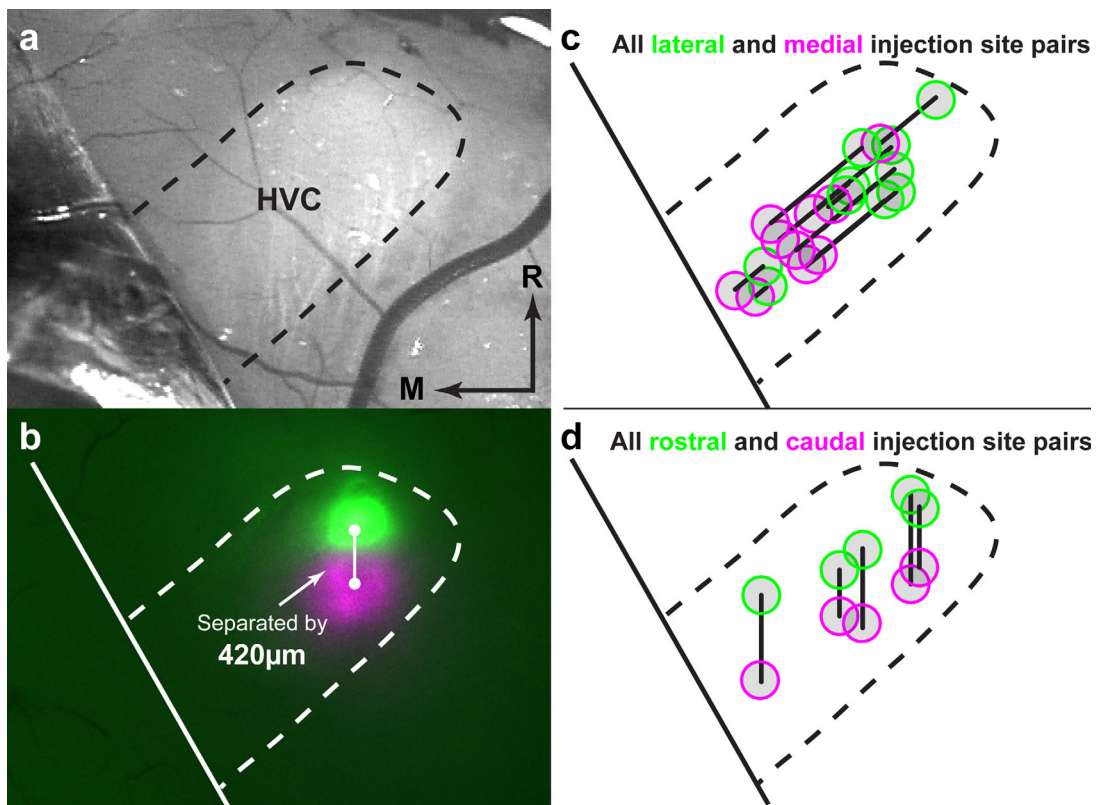
FIGURE 2   Dorsal views of the caudal telencephalon show HVC and the dual tracer injection sites. (a) An in vivo image captured during surgery shows resected dura mater in the bottom left and a heavily myelinated HVC in the center (outlined with a black dashed line). All paired tracer injections were visually-targeted using this general surgical approach. (b) Composite fluorescent image shows a rostral-caudal injection site pair in HVC (outlined with a white dashed line). The distance between injection sites is 420 μm. Schematic maps of the placements of all lateral-medial and all rostral-caudal HVC injection site pairs are shown in (c) and (d), respectively

implications for our understanding of the behavioral, physiological, and computational processes that encode the learned song within HVC.

2 | MATERIALS AND METHODS

2.1 | Animals and environment

Adult male zebra finches ($N = 12$, > 90 days post hatch), raised in our breeding aviaries, were housed singly in cages ($28.50 \times 21.00 \times 38.00$ cm) prior to surgery. Of this group, data from $N = 7$ birds were presented in Basista et al. (2014) to determine percent double-labeling relative to the distance between injection site pairs. However, except for a replotting these data in Figure 3, all other data from these birds are new.

Birds resided in a room with a 14h:10h (light:dark) photoperiod and a constant ambient temperature of 26 °C. We allowed 1 week for birds to acclimate to single-housing before tracer injections. Birds were provisioned daily with primarily millet-based assorted seed (400 Finch Blends, Jones Seed Company), a dietary supplement (Lafeber Finch Granules, Lafeber Company), water, and grit. All daily care procedures and experimental manipulations were reviewed and approved by the Florida State University Animal Care and Use Committee.

2.2 | In vivo injections of tracers into HVC

2.2.1 | Surgery

Experimental subjects were anesthetized via an intramuscular injection of Equithesin (0.045 cc) and then secured into a stereotaxic instrument. The skull was exposed by central incision of the scalp and retraction of the skin with curved forceps. Stereotaxic zero was set at the bifurcation of the mid-sagittal sinus. Phosphate buffered saline (PBS, 0.02 molar) was used to clean and hydrate the area. A large craniotomy was placed around the bifurcation of the midsagital sinus, encompassing the approximate bilateral location of HVC.

2.2.2 | Visualization of HVC

Tracer injection sites were selected by visualizing the dorsal surface of HVC. To visualize the dorsal surface of HVC, the dura-mater covering the caudal telencephalon was carefully resected. In the absence of dura, the heavy myelination of HVC was visible relative to the surrounding opaque brain tissue (Figure 2a). In $N = 6$ birds, resection of the dura was insufficient to definitively visualize HVC. For these birds, we resected the hippocampus over HVC, whereby the hippocampus covering the caudal nidopallium was unilaterally resected and pulled back medially toward the midsagital sinus, exposing HVC. In these birds, data were collected from the contralateral side only, where the
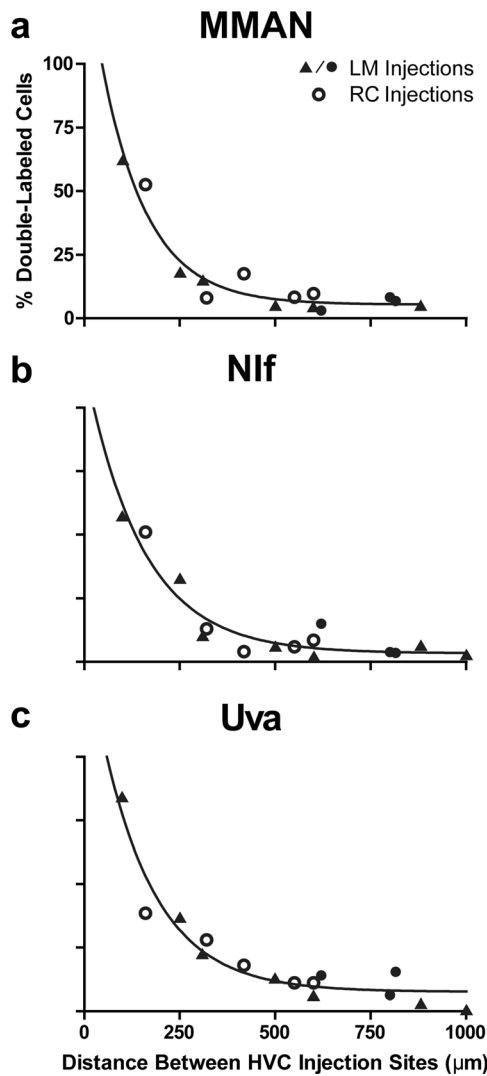
a MMAN

b NIf

c Uva

Distance Between HVC Injection Sites (μm)

FIGURE 3 Double-labeling in MMAN, NIf, and Uva decreases exponentially as a function of the distance between injection site pairs. Double-labeling of MMAN (a), NIf (b), and Uva (c) neurons is a function of the distance between, but not the axial orientation, of injection site pairs. Lateral-medial injection site pairs indicated with filled symbols and rostral-caudal injection site pairs indicated with open circles. Filled triangles are data replotted from Basista et al. (2014). The exponential decay function indicates that the axon terminals of MMAN, NIf, and Uva neurons narrowly target HVC locations that are defined by their rostral or caudal location within medial or lateral HVC. Note that one lateral-medial data point for MMAN (at 1,000 μm) was omitted due to tissue damage

hippocampus remained intact. Since HVC anatomy is bilaterally symmetrical, stereotaxic coordinates obtained from the hippocampus-exposed HVC side were used to direct injections into the hippocampus-intact side of HVC. Data collected from these $N = 6$ birds also confirmed that HVC extrinsic connectivity is exclusively ipsilateral. In the other $N = 6$ birds, HVC was targeted with tracer injections in both hemispheres. When tracer injections were confined to HVC, the clear majority of retrograde labeling was limited to MMAN, NIf, Uva, Av, and RA. However, in $N = 5$ hemispheres a small amount of one or both injected tracers extended below the ventral border of HVC, which produced some nidopallial and thalamic cell labeling around otherwise distinctly-labeled afferent nuclei (e.g., NIf in Figure 6d). Complete injection misses occurred in $N = 3$ hemispheres, bringing the total number of hemispheres used in this experiment to $N = 15$. Complete misses occurred below the ventral border of HVC, which cannot be visualized using the method described here.

2.2.3 | Tracer injections

Two different bidirectional fluorescent tracers, one with a red-emitting fluorophore and the other green-emitting, were injected into each HVC. Paired injections of DiI and DiO (5% in DMSO, Thermo Fisher Scientific Inc) or rhodamine and fluorescein conjugated dextran amines (3,000 molecular weight, Molecular Probes) were targeted to two separate HVC locations (see example in Figure 2b). The distance between the two injection sites varied between 0.1 and 1 mm for lateral-medial injections. For rostral-caudal HVC, the smaller length of this axis (~0.9 mm) limited the maximum distance between injection sites to 0.6 mm. Varying the distance between injection sites allowed us to estimate the spatial extent of afferent axonal terminals in HVC. For example, if a high percentage of cells were double-labeled when injection sites were placed at the extreme rostral and caudal edges of HVC, this would indicate that the terminations of individual afferent cells extended broadly across the rostral-caudal axis. Conversely, a low percentage of double-labeled cells when injection sites were placed at neighboring positions within HVC would indicate highly targeted terminations from individual afferent cells.

Tracers were delivered with glass micropipettes (World Precision Instruments, 1.2 mm outer diameter/0.68 mm inner diameter). Glass micropipettes were pulled using a vertical pipette puller (David Kopf Instruments Model 720) to a tip diameter of 15–20 μm, loaded with tracer by capillary action or gentle suction, and attached to a gas pressure injection system (Applied Scientific Instruments MPPI-3). Tracers were pressure-injected ($\leq$40 nl) at a depth of 0.45 mm from the dorsal surface of the brain. Tracer volume was estimated by determining the pressure and duration settings necessary to eject 40 nl of PBS drawn into a glass micropipette.

Birds received either lateral-medial or rostral-caudal injection site pairs into HVC. Figure 2c,d show the positions of all lateral-medial and rostral-caudal injection site pairs, respectively. The positions of rhodamine/DiI and fluorescein/DiO tracers were alternated across birds to validate labeling patterns. Moreover, injections of conjugated dextran amines in lateral-medial HVC ($N = 4$) and into rostral-caudal HVC ($N = 3$) were used to validate the pattern of labeling observed with DiI and DiO.

Birds were sacrificed 2–15 days postsurgery depending on the tracer. Birds were overdosed with equithesin (0.08 cc) and perfused intracardially with saline (20 ml), followed by ice-cold 4% paraformaldehyde (40 ml). Dissected brains were postfixed overnight in 4% paraformaldehyde, followed by PBS until sectioning. The telencephalon was then separated from the brainstem and each telencephalon was sectioned in the sagittal or coronal plane at 40 μm using a vibratome (Leica VT1000S). Each brainstem was sectioned in the sagittal plane at 40 μm.

2.3 | Imaging and analysis of tracer labeling

2.3.1 | Fluorescent imaging of labeled cells

All fluorescent images were captured using a digital camera (Optronics Mircofire) attached to a Leica DM5000B microscope. Serial sections containing nuclei that provide afferent input to HVC (i.e., MMAN, NIf, Uva, Av, RA) were mounted on glass slides, cover-slipped with saline to maintain section height, and immediately imaged with a 10x or 20x objective. Using Neurolucida 7.0 software (Microbrightfield Inc., RRID: SCR_001775), a set of images for both rhodamine/DiI and fluorescein/DiO tracers were captured at 5 µm intervals through the Z-axis of each nucleus in each section. Rhodamine/DiI and fluorescein/DiO image stacks were combined in Adobe Photoshop (Adobe Systems Inc., RRID: SCR_014199) to create a set of composite images that contained all single- and double-labeled cells.

Due to the small volumes of tracers that we injected into HVC the numbers of labeled cells in Av and RA were always small (<10 cells per section for RA, <20 cells per section for Av), regardless of which tracer pair we used. We therefore recorded qualitative observations of the labeling in Av and RA. Quantification and three-dimensional (3D) reconstruction were focused on MMAN, NIf, and Uva, nuclei where the population of labeled cells was large enough to reliably document systematic variation in the distribution of labeled cells as a function of injection site locations within HVC.

Following imaging, all sections were mounted onto microscope cover slides, dried, stained with thionin, and then coverslipped. Nissl-stained sections were used to validate the location and borders of the nuclei under study (HVC, MMAN, NIf, Uva, Av, RA,).

2.3.2 | Quantification of single- and double-labeled cells in MMAN, NIf, and Uva

Although care was taken to inject a similar volume of each dye into HVC, the total number of rhodamine dextran/DiI- or fluorescein dextran/DiO-labeled cells in each nucleus was rarely identical. Thus, in order to express the number of double-labeled (yellow) cells as a percentage, we first truncated the size of each single-labeled population to the smaller of the two populations. Therefore, the equation used is:

$$\frac{N_D}{2N_{Min\ (R\ or\ G)} + N_D}$$

where N_{min} is the number of the smallest population of single-labeled cells (either R = rhodamine/DiI or G = fluorescein/DiO) and N_D is the number of double-labeled cells. Both populations were then combined with the number of double-labeled cells to give the total number of labeled cells. Each labeled class of cells (rhodamine/DiI, fluorescein/DiO, and double-labeled) were then divided into the total number of labeled cells and converted to a percentage. We acknowledge that this approach is conservative and may slightly overestimate the percentage of double-labeled cells.

2.3.3 | Three-dimensional reconstruction of single- and double-labeled cells in MMAN, NIf, and Uva

The image stacks containing labeled cells for HVC afferent nuclei were loaded into Neurolucida, where the 3D position and tracer color (single-labeled rhodamine/DiI and fluorescein/DiO, or double-labeled yellow) of every cell was marked and saved as an ASCII file. To eliminate any potential bias for identifying the type and position of the tracers, all 3D reconstructions were completed by a group of individuals who were blind to injection site location. The borders of NIf and Uva—visible under both fluorescence and Nissl staining—were used to align the serial sections. However, MMAN lacks clear Nissl-defined borders. The distribution of labeled MMAN cells were, therefore, used to infer the shape of MMAN.

Each ASCII file was then loaded into Microsoft Excel, where data for the 3D position (X, Y, and Z axes) were separated into three two-dimensional (2D) plots (X/Y, Y/Z, and Z/X). 2D heat maps for each orientation were generated from these data using a specialized Matlab script (The Mathworks Inc., RRID: SCR_001622) containing the following algorithm. Letting (x_i, y_i)—where $i = 1, \ldots, n$ is a sequence of observations—we smoothed each 2D point using a 2D Gaussian kernel function. The smoothed heat map function is:

$$\sum_{i=1}^{n} \exp\left(-\frac{(x-x_i)^2 + (y-y_i)^2}{2\sigma^2}\right) \Big/ c$$

for any point (x, y), where σ is an appropriate bandwidth parameter, and c is a normalizing constant.

2.3.4 | Quantifying the peak density of cell labeling in MMAN, NIf, and Uva

While all sections containing the thalamus (Uva) were collected in the sagittal plane, we alternated the hemispheric plane of section for both lateral-medial and rostral-caudal injection site pairs to better visualize potential topography in the retrograde labeling within MMAN and NIf. In general, we noted topography in MMAN when hemispheres with lateral-medial injection pairs were sectioned in the coronal plane (N = 6), and in NIf when rostral-caudal injections were sectioned in the sagittal plane (N = 4). We also sectioned a subset of hemispheres orthogonal to injection site pairs: lateral-medial injections were sectioned in the sagittal plane (N = 3), and a rostral-caudal hemisphere was sectioned in the coronal plane (N = 1). We found that this procedure did not reveal any visually-apparent topography.

To quantify population-level patterns of retrograde labeling within MMAN, NIf, and Uva, we calculated the spatial location of peak density within the distribution of each labeled cell population. To calculate these values, we first centered the 2D excel data points that represent the total population of labeled cells for each nucleus. Centering was accomplished by subtracting the x and y (x,y) position for each data point from the mean of all data points (mean of x, mean of y). This centered each nucleus (to 0,0) and allowed us to combine all nuclei for subsets of birds that shared axial orientation and distance separating injection site pairs (e.g., MMAN for all birds where lateral-medial HVC tracer injection pairs are separated by ≥600 µm). Peak density values were obtained from the output of the Gaussian kernel function above, where maximum values represent the position of highest cell density. The 2D positions of these maximum values were calculated for MMAN, NIf, and Uva, then averaged across subsets of birds with similar HVC injection site pairs.

3 | RESULTS

We previously identified distinct populations of MMAN, NIf, Uva, and RA neurons that target either lateral HVC or medial HVC (Basista et al., 2014). Here, toward a more comprehensive examination of HVC input connectivity across both lateral-medial and rostral-caudal axes, we quantified the 3D pattern of retrograde labeling within MMAN, NIf, and Uva as a function of the orientation (lateral-medial or rostral-caudal) and the distance between (ranging from 0.1 to 1 mm) HVC injection site pairs. Thus, the independent variables in this experiment were the orientation and the distance between injection site pairs.

Figure 2b shows a representative example of an injection site pair, oriented across the rostral-caudal axis and separated by 420 μm. As is apparent in this image, there was variation in the amount of tracer diffusion away from the two injection sites. Because tracer concentration falls with increasing diffusion away from the injection site, we could not be certain that tracer concentrations near the edges of the diffusion border would be sufficient for retrograde labeling. Therefore, all double-labeling data are expressed in terms of the distance between the placements of tracer injection micropipettes, where we can be certain that tracer concentrations were sufficient for labeling.

3.1 | The distance between injection site pairs, but not their axial orientation, determines the percentage of double-labeled cells in MMAN, NIf, and Uva

As we found for lateral-medial HVC injection site pairs (Basista et al., 2014), the distance between rostral-caudal HVC injection site pairs determined the percentage of double-labeled cells in MMAN, NIf, and Uva. In Figure 3 we replot data from Basista et al. (2014, closed triangles, $N = 7$) along with new lateral-medial (closed circles, $N = 3$) and rostral-caudal injection site pairs (open circles, $N = 5$). A pattern of exponential decay holds for both axial orientations when plotting percent double-labeled cells as a function of distance between injection site pairs (R^2 values for exponential decay regressions are MMAN = 0.93, NIf = 0.91, and Uva = 0.92). Moreover, the distance at which the exponential decay functions flatten (400–500 μm between injection site pairs, Figure 3a–c) indicates that the terminals from each afferent neuron target specific rostral or caudal locations within medial or lateral HVC. By squaring the distance at which cells become predominately single-labeled (400–500 μm) we estimate that the axon terminals of individual MMAN, NIf, and Uva neurons each occupy an area of 0.16–0.25 mm^2. Although this estimate is conservative, it is nevertheless clear that terminals from each MMAN, NIf, and Uva neuron address only one rostral or caudal location within medial or lateral HVC, and that each HVC location receives convergent input from each afferent nucleus in parallel. Note that we did not investigate the comparatively thin dorsal-ventral axis of HVC, and it is possible that a further targeting of afferent input occurs within this axis.

3.2 | Quantifying the distributions of labeled cells reveals population-level topography in MMAN and NIf, but not Uva

Earlier studies of HVC input connectivity used injections of a single tracer, and these investigators reported an absence of topography in the organization of MMAN, NIf, and Uva input to HVC (Bottjer et al., 1989; Fortune & Margoliash, 1995; Foster & Bottjer, 1998; Nottebohm et al., 1982). Indeed, when using two different tracers we observed overlapping distributions of single-labeled cells in MMAN, NIf, and Uva regardless of injection site placements. However, while the overlapping distributions of cells within each nucleus suggested no overt topography, we identified visually apparent biases in the distribution density of single-labeled cells that suggested a possible population-level topographic organization in MMAN and NIf. That is, while the position of any one labeled cell within MMAN or NIf did not reliably predict the location of the injection site in HVC, the distribution density of the entire labeled population appeared to consistently reflect the location of the HVC injection site. To elucidate and quantify these biases, we generated density-based heat maps using the 3D position of each single-labeled cell in MMAN, NIf, and Uva of each bird.

3.2.1 | MMAN input to HVC features population-level topography across the lateral-medial axis

Figure 4 shows single-subject and summary data for MMAN labeling following paired tracer injections across the lateral-medial or rostral-caudal axis of HVC. For reference, Figure 4a shows a coronal schematic of the shape and position of the cortical nucleus MMAN (outlined in the dashed box) and Figure 4c shows a representative example of MMAN labeling when the brain was sectioned in the coronal plane. This bird received lateral (magenta) and medial (green) tracer injections, separated by 815 μm, into HVC. While there is substantial overlap between both labeled cell populations, there is an apparent bias in the density of single-labeled cells: the lateral half of MMAN contains a greater density of cells labeled with the tracer injected into lateral HVC (magenta), and the medial half of MMAN contains a greater density of cells labeled with the tracer injected into medial HVC (green). Figure 4e shows 3D reconstructions of magenta and green cell labeling in alternate MMAN sections from this bird, as well as the resulting heat maps. Each row presents serial sections from a different orientation (Sagittal, Dorsal, and Coronal), for both lateral and medial injections. The points representing individual cells can be seen in the first two columns, and their corresponding heat maps are shown in the neighboring two columns. The lateral injection labeled a greater percentage of cells in the lateral half of MMAN (62% of cells in the lateral half of MMAN contain dye from the lateral HVC injection). In contrast, the medial injection labels a greater percentage of cells in the medial half of MMAN (81% of cells in the medial half of MMAN contain dye from the medial HVC injection). While the sagittal heat maps show density peaks near the center of MMAN, the dorsal and coronal heat maps show clear lateral and medial peaks in the density of labeled cells, confirming a population-level topography across the lateral-medial axis for this bird.

To determine whether these results were consistent across all birds with similar lateral-medial HVC injection site pairs, we generated a coronal composite of MMAN ($N = 5$ birds) and calculated mean peak densities for the two populations of single-labeled cells. The composite MMAN in Figure 4g contains all single-labeled MMAN cells produced by lateral-medial HVC injection site pairs separated by $\geq 600\,\mu m$. For purposes of illustration, all cells labeled by lateral HVC injections are shown in magenta and all cells labeled by medial HVC injections are

shown in green (tracer fluorophores were reversed in some birds, see Methods). The mean peak densities of MMAN cells projecting to lateral (magenta) or medial (green) HVC are indicated with large x̄ circles. Figure 5a shows group mean and individual subject data for this comparison, where the lateral-medial difference in peak density is apparent for each subject. A paired t-test showed a statistically reliable difference between the mean peak densities of the two labeled cell populations ($t_4 = 4.69$, $p < .01$). These results confirm the lateral-medial topography
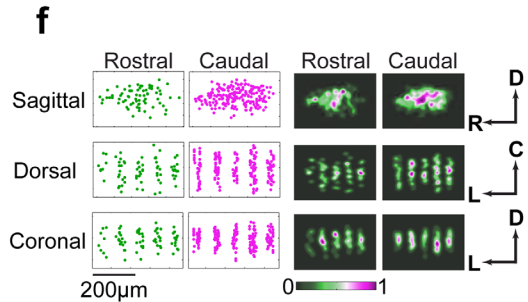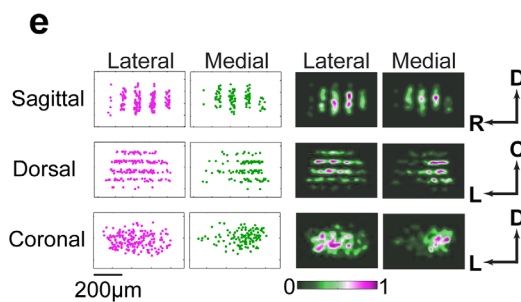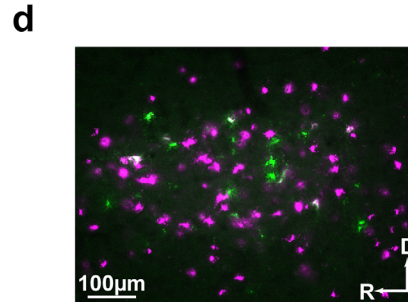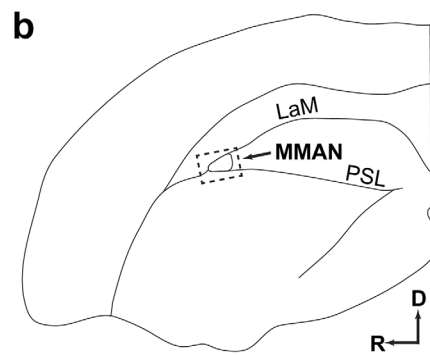
MMAN labeling
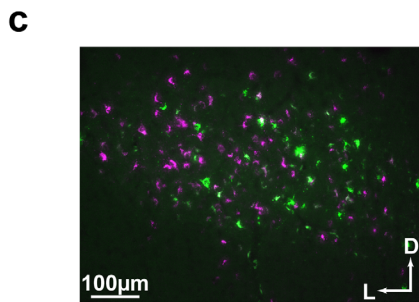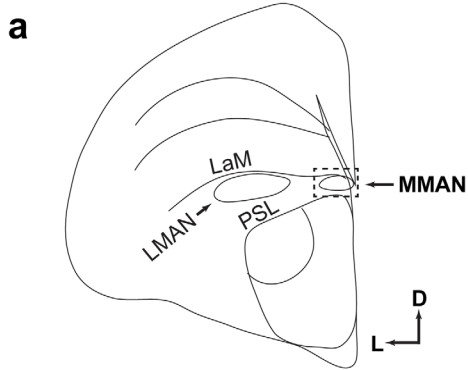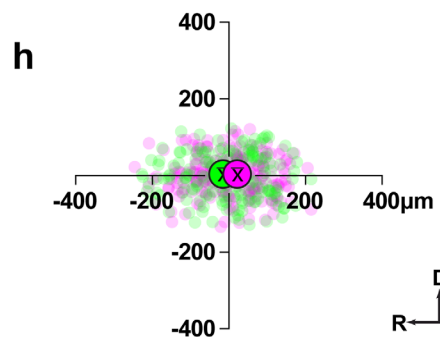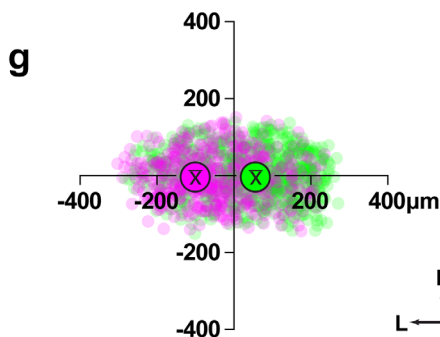
FIGURE 4.

observed in Figure 4c,e, and indicate that this pattern is a general property of MMAN input to HVC in adult birds.

3.2.2 | MMAN input to HVC lacks population-level topography across the rostral-caudal axis

We also examined whether MMAN input to HVC displays population-level topography across the rostral-caudal axis. Figure 4b shows a schematic sagittal brain section containing MMAN (outlined in the dashed box). In Figure 4d, we show a representative sagittal MMAN section from a bird with rostral (green) and caudal (magenta) HVC injections separated by 550 μm. Like lateral-medial HVC injection site pairs, we found substantial overlap in populations of single-labeled cells throughout MMAN. However, we did not observe any topographic bias in the distribution density of labeled cells in this or any other sagittal section containing MMAN. Figure 4f shows 3D reconstructions of magenta and green cell labeling in all MMAN sections from this bird, as well as the resulting heat maps. No population-level topography across any axis is observed.

To determine whether these results were consistent across all birds with similar rostral-caudal HVC injection site pairs, we generated a sagittal composite of MMAN ($N = 4$ birds) and calculated mean peak densities for the two populations of single-labeled cells. The composite MMAN in Figure 4h contains all single-labeled cells produced by rostral-caudal HVC injection site pairs that were separated by ≥ 320 μm. The mean peak densities of MMAN cells labeled by rostral (green) or caudal (magenta) HVC tracer injections show little deviation from the center of MMAN. Figure 5b shows group mean and individual subject data for this comparison, where no consistent trend for a rostral-caudal difference in peak density is observed across individual subjects. Moreover, a paired t-test indicated a lack of population-level topography in MMAN input across the rostral-caudal axis of HVC ($t_3 = 1.14$, $p = .34$).

Together, the results from Figures 4 and 5a,b indicate that population-level topography in MMAN input to HVC is organized exclusively across the lateral-medial axis. The known importance of MMAN for juvenile song learning (Foster & Bottjer, 2001) suggests a role for topographic MMAN input in the differential development of lateral and medial HVC, which appear to play distinct roles in encoding the adult song (Basista et al., 2014).

3.2.3 | NIf input to HVC lacks population-level topography across the lateral-medial axis

As with MMAN, we examined whether NIf input to HVC displays population-level topography across the lateral-medial and/or rostral-caudal axes of HVC. Figure 6a shows a schematic coronal brain section with the cortical nucleus NIf (outlined in the dashed box) and Figure 6c shows a representative coronal section containing NIf from a bird where lateral (magenta) and medial (green) HVC injection sites were separated by 880 μm. There is substantial overlap in both populations of cells, but no apparent topographic biases in the distribution density of either population of single-labeled cells. The 3D reconstructions in Figure 6e confirm the lack of population-level topography in the density of labeled cells across any axis.

To determine whether these results were consistent across all birds with similar lateral-medial HVC injection site pairs, we generated a coronal composite of NIf ($N = 6$ birds) and calculated mean peak densities for the two populations of single-labeled cells. The composite NIf in Figure 6g contains all single-labeled cells produced by lateral-medial HVC injection site pairs separated by ≥ 600 μm. The mean peak densities of NIf cells labeled by lateral (magenta) or medial (green) HVC tracer injections show little deviation from the center of NIf. Figure 5c shows group mean and individual subject data for this comparison, where no consistent trend for a lateral-medial difference in peak density is observed across individual subjects. Moreover, a paired t-test indicated a lack of population-level topography in NIf input across the lateral-medial axis of HVC ($t_5 = 0.63$, $p = .56$). These results indicate NIf input to HVC lacks population-level topography across the lateral-medial axis.

3.2.4 | NIf input to HVC features an inverse population-level topography across the rostral-caudal axis

Figure 6b shows a schematic sagittal brain section containing NIf (outlined in the dashed box). Sagittal NIf sections, such as the representative

FIGURE 4 MMAN input to HVC shows exclusive topographic connectivity across the lateral-medial axis. Schematic sections show the position and shape of MMAN within the medial portion of the anterior nidopallium, from coronal (a) and sagittal (b) perspectives. Magenta and green cells in (c, e, g) are from lateral and medial HVC injection sites, respectively. Green and magenta cells in (d, f, h) are from rostral and caudal HVC injection sites, respectively. The coronal tissue section in (c) shows topography in the distribution of single-labeled MMAN neurons following tracer injections into lateral (rhodamine dextran) and medial (fluorescein dextran) HVC. In contrast, the sagittal tissue section in (d) shows no apparent topography in the distribution of single-labeled MMAN neurons following tracer injections into rostral (fluorescein dextran) and caudal (rhodamine dextran) HVC. (e, f) Heat maps generated from alternate sections show the overall patterns of nuclear labeling from (c) and (d), respectively. Each row represents a different 2D axis of MMAN (Sagittal, Dorsal, and Coronal). Each magenta and green data point in the first two columns represent individual single-labeled cells within MMAN. The last two columns show heat maps produced from the first two columns. On each heat map, magenta represents regions of peak cell density within MMAN. Dorsal and coronal views in (e) show peak densities for rhodamine dextran- and fluorescein dextran-labeled neurons within lateral and medial MMAN, respectively, confirming a lateral-medial topography. In (f), no topographic bias in the peak density of labeled cells is apparent across any 2D axis, confirming the lack of rostral-caudal topography. (g) A coronal composite MMAN contains all single-labeled cells from a group of birds ($N = 5$) that received lateral-medial HVC injection site pairs (separated by ≥ 600 μm). Coordinates for the mean peak densities of the two populations of labeled cells are indicated by large magenta and green $\bar{x}$ circles, demonstrating a population-level topography across the lateral-medial axis of MMAN. See Figure 5a for statistical comparison. (h) A sagittal composite MMAN contains all single-labeled cells from a group of birds ($N = 4$) that received rostral-caudal HVC injection site pairs (separated by ≥ 320 μm). Coordinates for the mean peak densities of the two populations of labeled cells are indicated by large green and magenta $\bar{x}$ circles, and demonstrate the lack of a population-level topography across the rostral-caudal axis of MMAN. See Figure 5b for statistical comparison
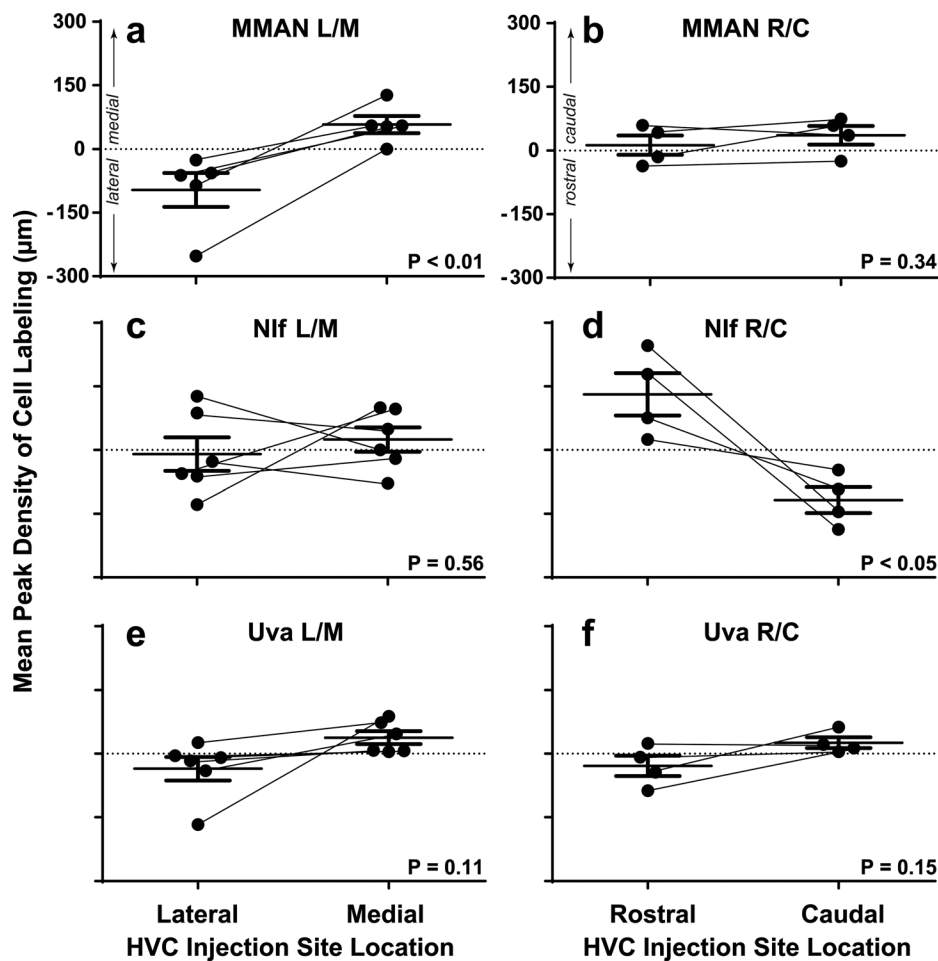
FIGURE 5 Locations of the mean peak density of cell labeling in MMAN, NIf, and Uva following paired tracer injections across the lateral-medial (L/M) or rostral-caudal (R/C) axis of HVC. MMAN (a, b) Group mean and individual subject data demonstrate a statistically significant topography across the lateral-medial axis (a) of MMAN. Data are from $N = 5$ birds where lateral-medial HVC injection site pairs were separated by $\geq 600\,\mu m$. Note that topography is observed in all individual subjects. In contrast, no rostral-caudal MMAN topography was observed in $N = 4$ birds (b) where rostral-caudal HVC injection site pairs were separated by $\geq 320\,\mu m$. NIf (c, d): Group mean and individual subject data demonstrate an absence of lateral-medial NIf topography (c) in $N = 6$ birds where lateral-medial HVC injection site pairs were separated by $\geq 600\,\mu m$. In contrast, a statistically significant topography is observed across the rostral-caudal axis (d), albeit inversely. Data are from $N = 4$ birds where rostral-caudal HVC injection site pairs were separated by $\geq 320\,\mu m$. Note that topography is observed in all individual subjects. Uva (e, f): Group mean data reveal no statistically significant topography across either axis—lateral-medial (e) or rostral-caudal (f). Lateral-medial data are from $N = 6$ birds that received lateral-medial HVC injection site pairs that were separated by $\geq 600\,\mu m$. Rostral-caudal data are from $N = 4$ birds that received rostral-caudal HVC injection site pairs that were separated by $\geq 320\,\mu m$. Interestingly, individual subject data suggest a small trend for Uva topography across both axes. A larger sample may be necessary to detect what appear to be small but potentially reliable differences. Error bars in all graphs are SE

example in Figure 6d, reveal an inverse topographic bias in the density of single-labeled cells. Here, a bird that received rostral (green) and caudal (magenta) tracer injections into HVC (separated by 550 μm) shows an apparent bias for caudal HVC-projecting cells within the rostral half of NIf, and rostral HVC-projecting cells within the caudal half of NIf. The 3D reconstructions in Figure 6f confirm this observation: although there is substantial overlap between both labeled cell populations, the rostral injection labeled a greater density of cells in the caudal half of NIf (69% of caudal NIf cells contain dye from the rostral HVC injection). In contrast, the caudal injection labeled a greater density of cells in the rostral half of NIf (65% of rostral NIf cells contain dye from the caudal HVC injection). These data suggest that NIf possesses a population-level

topography across, and inverse to, the rostral-caudal axis of HVC in this bird.

To determine whether these results were consistent across all birds with similar rostral-caudal HVC injection site pairs, we generated a sagittal composite of NIf ($N = 4$ birds) and calculated mean peak densities for the two populations of single-labeled cells. The composite NIf in Figure 6h contains all single-labeled cells produced by rostral-caudal HVC injection site pairs separated by $\geq 320\,\mu m$. Figure 5d shows group mean and individual subject data for this comparison, where the rostral-caudal difference in peak density is apparent for each subject. A paired t test showed a statistically reliable difference between the mean peak densities of the two labeled cell populations ($t_3 = 3.22$, $p < .05$).

Together, the results from Figures 6 and 5c,d indicate an inverse population-level topography in NIf input to HVC that is organized exclusively across the rostral-caudal axis. The known importance of NIf for juvenile song learning (Naie & Hahnloser, 2011; Piristine, Choetso, & Gobes, 2016) suggests a role for topographic NIf input in differentially influencing activity across the rostral-caudal axis of HVC during learning. It is also worth noting here that the topographies of MMAN and NIf input are arranged orthogonal to each other (lateral-medial for MMAN, rostral-caudal for NIf, compare Figures 4 and 6).
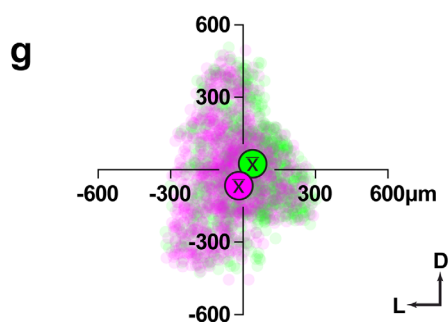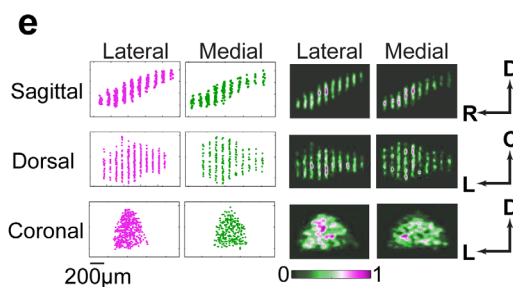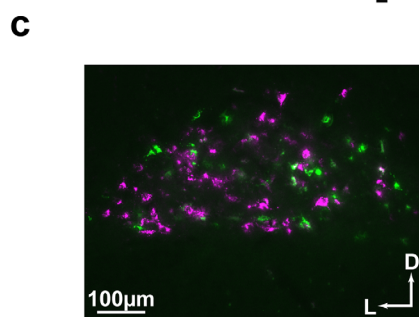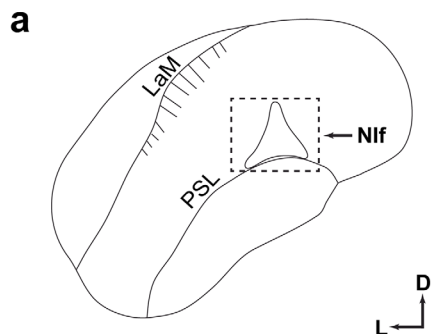
3.2.5 | Uva input to HVC appears to lack population-level topography

Unlike MMAN and NIf, visual inspection of single-labeled cell populations in Uva provided little hint of topography across any axis. For reference, Figure 7a,b show schematic coronal and sagittal views of the thalamic nucleus Uva, respectively. However, the reader is reminded here that all Uva sections were collected in the sagittal plane, which may have prevented visual discernment of topography across the lateral-medial axis. Indeed, no topography is observed in the sagittal
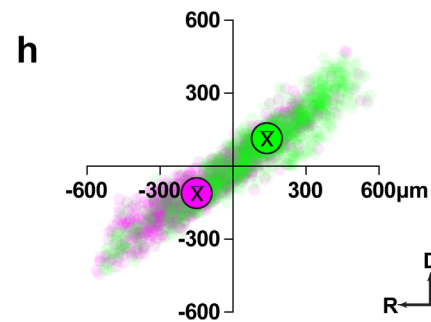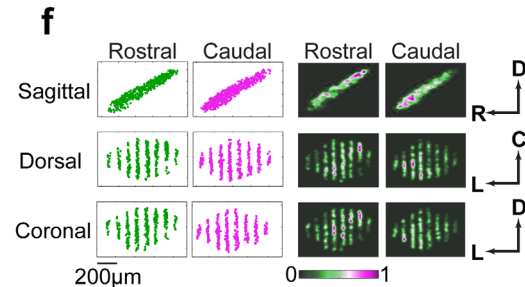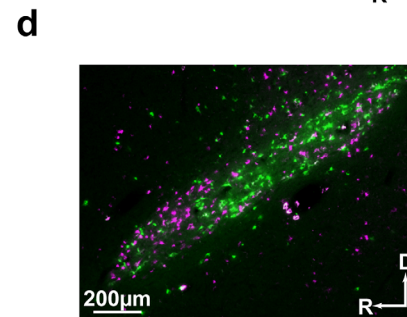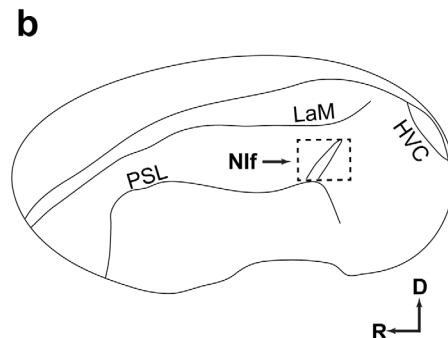

FIGURE 6.

section of Uva shown in Figure 7c, which was taken from a bird where lateral (magenta) and medial (green) HVC injection sites were separated by 815 μm. However, the 3D reconstructions for this bird (Figure 7e) show no clear topographic pattern for either single-labeled cell population, particularly within the coronal plane where one might expect lateral-medial topography to emerge. Similarly, Figure 7d shows a representative sagittal section of Uva from a bird where rostral (magenta) and caudal (green) HVC injection sites were separated by 550 μm. No topography is apparent even though the plane of section (sagittal) is aligned to the rostral-caudal axis. The 3D reconstructions for this bird (Figure 7f) also show no differences in the density peaks for either single-labeled cell population.

Summary data confirmed the apparent lack of topography in Uva input to HVC. For example, Figure 7g shows a coronal composite of Uva (N = 6 birds) containing all single-labeled cells produced by lateral-medial HVC injection site pairs separated by ≥600 μm. The mean peak densities for lateral- (magenta) and medial- (green) labeled cells show little deviation from the center of the composite Uva. Similarly, Figure 7h shows a sagittal composite of Uva (N = 4 birds) containing all single-labeled cells produced by rostral-caudal HVC injection site pairs separated by ≥320 μm. The mean peak densities for rostral (magenta) and caudal (green) cells show little deviation from the center of the composite Uva.

Group mean and individual subject data for the Uva labeling data are shown in Figure 5e,f. Although we found little visual evidence for population-level topography in the pattern of Uva input HVC, quantification of the labeling data appears to show a trend for topography across both lateral-medial and rostral-caudal axes. While mean peak differences in cell density failed to reach statistical significance in both comparisons (medial-lateral, $t_5 = 1.92$, $p = .11$; rostral-caudal, $t_3 = 1.91$, $p = .15$), a larger sample with greater statistical power may be necessary to detect what could be small but reliable differences. Another consideration is that our volumes of injected tracer (≤40 nl) may have been too large to detect population-level topography within the round shape and small volume of Uva (e.g., Uva is approximately 1/5th

the volume of NIf). If smaller volumes of tracer were used it is possible that a more prominent topography might emerge.

In Basista et al. (2014) we found that a greater proportion of Uva neurons target lateral HVC over medial HVC when lateral-medial injection site pairs were separated by ≥600 μm (N = 3). Here, we reanalyzed this distinctive pattern of Uva labeling with additional birds (N = 2) and obtained a similar result. Compared to the average ratio of MMAN and NIf cells that targeted either lateral or medial HVC, Uva cells were 2.2 times more likely to target lateral over medial HVC. We also asked if Uva cells showed a preferential targeting for rostral or caudal HVC. Compared to the average ratio of MMAN and NIf cells that targeted either rostral or caudal HVC, Uva cells were nearly equally likely (ratio of 1.07:0.93) to target rostral HVC as caudal HVC (N = 4). That is, Uva was the only afferent nucleus to show a systematic difference in the number of labeled cells as a function of injection site location. Although the pattern of Uva input to HVC appears to lack topography, the preferential targeting of lateral HVC may reflect the distinct role of lateral HVC in encoding the adult song (Basista et al., 2014).

3.3 | Av cells also target specific HVC loci in parallel

We also examined whether Av cells target distinct HVC loci. Although the small number of Av cells labeled by our focal tracer injections precluded quantitative analysis of topography (larger tracer injections are necessary to more completely label Av, see Akutagawa & Konishi, 2010), the Av labeling we observed is shown for two birds in Figure 8. Av sits in the caudal mesopallium (CM) immediately dorsal to the mesopallial lamina (LaM, outlined in white) that separates nidopallium from mesopallium; NIf is shown in the images for reference. Figure 8a,b shows a sagittal tissue section from a bird where lateral (magenta) and medial (green) HVC injection sites were separated by 500 μm, while Figure 8c,d shows a sagittal tissue section from a bird where rostral (magenta) and caudal (green) HVC injection sites were separated by 600 μm. These images show that Av cells are predominantly single-labeled, like MMAN, NIf, and Uva cells from the same birds. These

FIGURE 6 NIf input to HVC shows exclusive, inverse topographic connectivity across the rostral-caudal axis. Schematic sections show the position and shape of NIf within the caudal nidopallium, from coronal (a) and sagittal (b) perspectives. Magenta and green cells in (c, e, g) are from lateral and medial HVC injection sites, respectively. Green and magenta cells in (d, f, h) are from rostral and caudal HVC injection sites, respectively. The coronal tissue section in (c) shows no apparent topography in the distribution of single-labeled NIf neurons following tracer injections into lateral (DiI) and medial (DiO) HVC. In contrast, the sagittal tissue section in (d) shows an inverse topography in the distribution of single-labeled NIf neurons following tracer injections into rostral (fluorescein dextran) and caudal (rhodamine dextran) HVC. (e, f) Heat maps generated from alternate NIf sections show the overall patterns of nuclear labeling from (c) and (d), respectively. Each row represents a different 2D axis of NIf (Sagittal, Dorsal, and Coronal). Each magenta and green data point in the first two columns represent individual single-labeled cells within NIf. The last two columns show heat maps produced from the first two columns. On each heat map, magenta represents regions of peak cell density within NIf. In (e), no topographic bias in the peak density of labeled cells is seen across any 2D axis, confirming the lack of lateral-medial topography. In (f), the sagittal view shows peak densities for magenta- and green-labeled neurons within rostral and caudal NIf, respectively, confirming an inverse rostral-caudal topography. (g) A coronal composite NIf contains all single-labeled cells from a group of birds (N = 6) that received lateral-medial HVC injection site pairs (separated by ≥ 600 μm). Coordinates for the mean peak densities of the two populations of labeled cells are indicated by large magenta and green x̄ circles, demonstrating the lack of topography across the lateral-medial axis of NIf. See Figure 5c for statistical comparison. (h) A sagittal composite NIf contains all single-labeled cells from a group of birds (N = 4) that received rostral-caudal HVC injection site pairs (separated by ≥ 320 μm). Coordinates for the mean peak densities of the two populations of labeled cells are indicated by large magenta and green x̄ circles, demonstrating an inverse topography across the rostral-caudal axis of NIf. See Figure 5d for statistical comparison

observations suggest that distinct subpopulations of Av cells (like MMAN, Nlf, and Uva cells) each target specific lateral, medial, rostral, or caudal locations within HVC in parallel.

In contrast to a previous report of a general input from CM to HVC (Bauer et al., 2008), we found few labeled cells in the CM outside of Av. This would lend support to Akutagawa and Konishi's (2010) hypothesis that most CM connections to HVC likely originate from Av.

3.4 | Bidirectional connectivity between HVC and RA maintains a parallel organization

Using lateral-medial HVC injection site pairs we previously reported that lateral and medial HVC send distinct, parallel streams of axons to RA, and that reciprocal connectivity from RA to HVC is also organized in parallel (Figure 9a in Basista et al., 2014). Here, we examined the pattern of bidirectional labeling between HVC and RA following
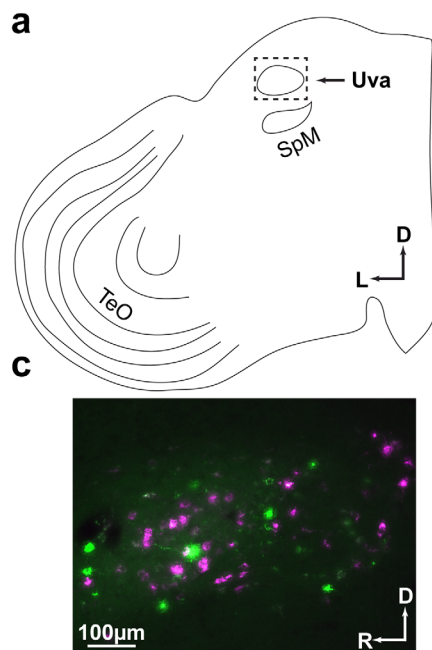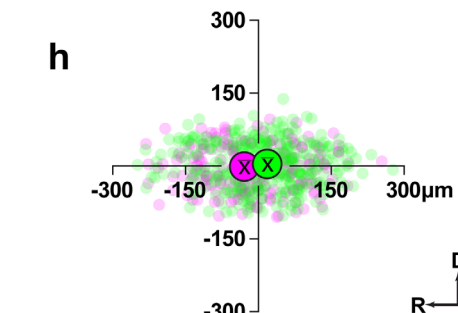
FIGURE 7.

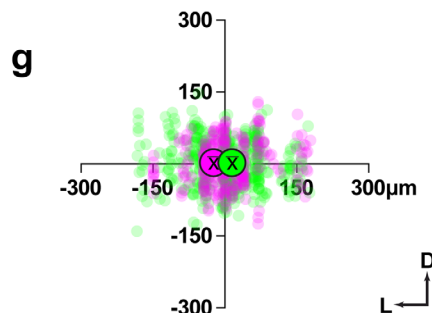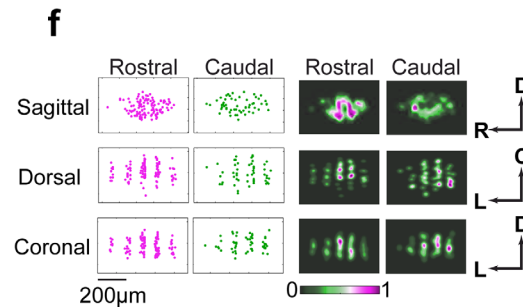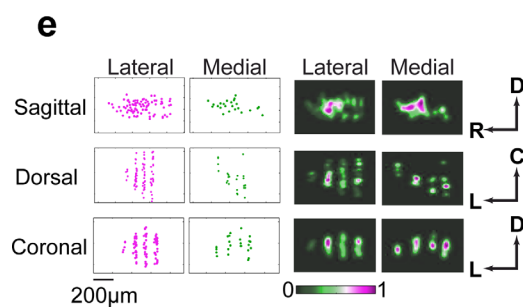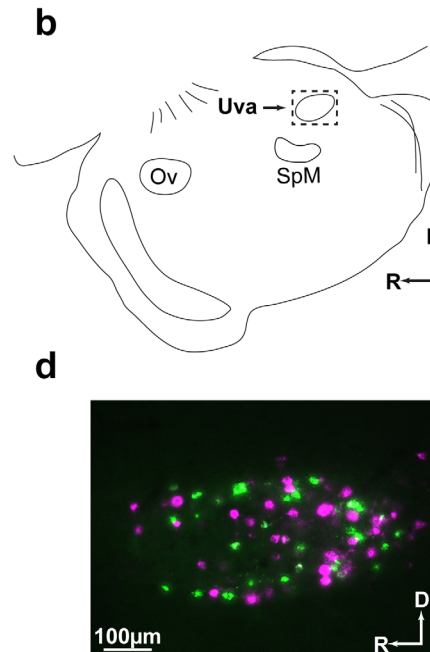rostral-caudal HVC injection site pairs. Figure 9 shows a representative example from a bird where rostral (magenta) and caudal (green) HVC injection sites were separated by 420 μm. The presence of only one (magenta or green) label in HVC fiber bundles indicates that each fiber bundle originates from either rostral or caudal HVC. As with HVC axons labeled following lateral-medial HVC injections (Basista et al., 2014), we found that the terminal arborizations of rostral and caudal HVC axons overlap one another and are distributed throughout vocal-motor cortex, RA. Thus, RA neurons appear to be a site of convergence for the multiple, parallel streams of axons emanating from lateral, medial, rostral, and caudal HVC.

The asterisks in Figure 9 highlight single-labeled (magenta or green) RA-HVC cells that have reciprocal-connectivity with rostral or caudal HVC. This pattern of single labeling of RA-HVC cells is identical to what we observed following lateral-medial tracer injections into HVC (Basista et al., 2014). As with Av (Figure 8), only small numbers of RA-HVC cells were labeled by our focal tracer injections, precluding quantitative analysis of topography (larger tracer injections are necessary to more completely label the population of RA-HVC cells, see Roberts et al., 2008). However, as the example in Figure 9 shows, RA-HVC cells are predominantly single-labeled, like MMAN, NIf, and Uva cells from the same bird. These observations suggest that distinct subpopulations of RA-HVC cells (like MMAN, NIf, Uva, and Av cells) each target specific lateral, medial, rostral, or caudal locations within HVC in parallel.

3.5 | Terminal labeling of HVC neurons that project to Area X

Like injection site pairs into lateral and medial HVC (Basista et al., 2014), we found that injection site pairs in rostral and caudal HVC provided faint labeling of the axon terminals of HVC neurons that project to Area X (data not shown). Like anterograde transport to RA, labeling appeared to fill the entire volume of Area X, and no discernable topography was observed. However, the terminal labeling in Area X was consistently quite faint relative to RA, likely due to the smaller volume of RA (Area X is roughly 6 times the volume of RA) and the 4-times-larger population of HVC neurons that project to RA (Wild, Williams, Howie, & Mooney, 2005). Thus, while our focal tracer injections were sufficient to provide intense labeling of HVC axon terminals within RA, we suspect that larger injections would be necessary to produce labeling of equivalent intensity within Area X.

4 | DISCUSSION

When combined with previous findings (Basista et al., 2014), the present results reveal a massively parallel input architecture for HVC. By varying the axial orientation and distance between focal HVC injection site pairs, we find that each afferent nucleus (MMAN, NIf, Uva, Av, and RA) contains multiple cell populations targeting multiple HVC locations in parallel. In turn, each HVC location extends isolated bundles of efferent axons to RA, where the terminal arborizations ramify, overlapping one another and filling the volume of RA. Moreover, for MMAN and NIf, quantifying the distributions of single-labeled cells as a function of the axial orientation of the HVC injection site pairs reveals an orthogonal topography. Whereas MMAN input to HVC shows organization across the lateral-medial axis, NIf input to HVC shows organization across the rostral-caudal axis, albeit inversely. Importantly, our findings explain why it appeared to previous investigators that the input architecture of HVC lacked topography or a specific organization of any kind (Akutagawa & Konishi, 2010; Bottjer et al., 1989; Foster & Bottjer, 1998; Fortune & Margoliash, 1995; Nottebohm et al., 1982). The findings of these earlier studies, all based on injections of a single tracer into HVC, can be understood by examining the widespread distribution of one or the other population of single-labeled cells in MMAN or NIf (Figures 4 and 6). Clear evidence of a parallel and topographic organization only emerges by quantifying the distribution densities of the two populations of single-labeled cells produced by paired tracer injections into HVC.

FIGURE 7 Uva input to HVC appears to lack topography. Schematic sections show the position and shape of Uva within the thalamus, from coronal (a) and sagittal (b) perspectives. Magenta and green cells in (c, e, g) are from lateral and medial HVC injection sites, respectively. Green and magenta cells in (d, f, h) are from rostral and caudal HVC injection sites, respectively. In (c), no apparent topography is observed in a sagittal tissue section following tracer injections into lateral (rhodamine dextran) and medial (fluorescein dextran) HVC. However, note that the sagittal plane of section may have obscured lateral-medial topography (but see coronal plane in e). In (d) no apparent topography is observed in a sagittal tissue section following tracer injections into rostral (rhodamine dextran) and caudal (fluorescein dextran) HVC. (e, f) Heat maps generated from alternate Uva sections show the overall patterns of nuclear labeling from (c) and (d), respectively. Each row represents a different 2D axis of Uva (Sagittal, Dorsal, and Coronal). Each magenta and green data point in the first two columns represent individual single-labeled cells within NIf. The last two columns show heat maps produced from the first two columns. On each heat map, magenta represents regions of peak cell density within Uva. (e) No apparent topography is observed in any plane of section, including the coronal plane where lateral-medial topography would be expected to emerge. (f) No apparent topography is observed in any plane of section, including the sagittal plane where rostral-caudal topography would be expected to emerge. (g) A coronal composite Uva contains all single-labeled cells from a group of birds (N = 6) that received lateral-medial HVC injection site pairs (separated by ≥ 600 μm). Coordinates for the mean peak densities of the two populations of labeled cells are indicated by large magenta and green x̄ circles, demonstrating the apparent lack of topography across the lateral-medial axis of Uva. However, note that the individual subject data in Figure 5e suggest a small trend in lateral-medial topography. (h) A sagittal composite Uva contains all single-labeled cells from a group of birds (N = 4) that received rostral-caudal HVC injection site pairs (separated by ≥ 320 μm). Coordinates for the mean peak densities of the two populations of labeled cells are indicated by large magenta and green x̄ circles, demonstrating the apparent lack of topography across the rostral-caudal axis of Uva. However, note that the individual subject data in Figure 5f suggest a small trend in rostral-caudal topography
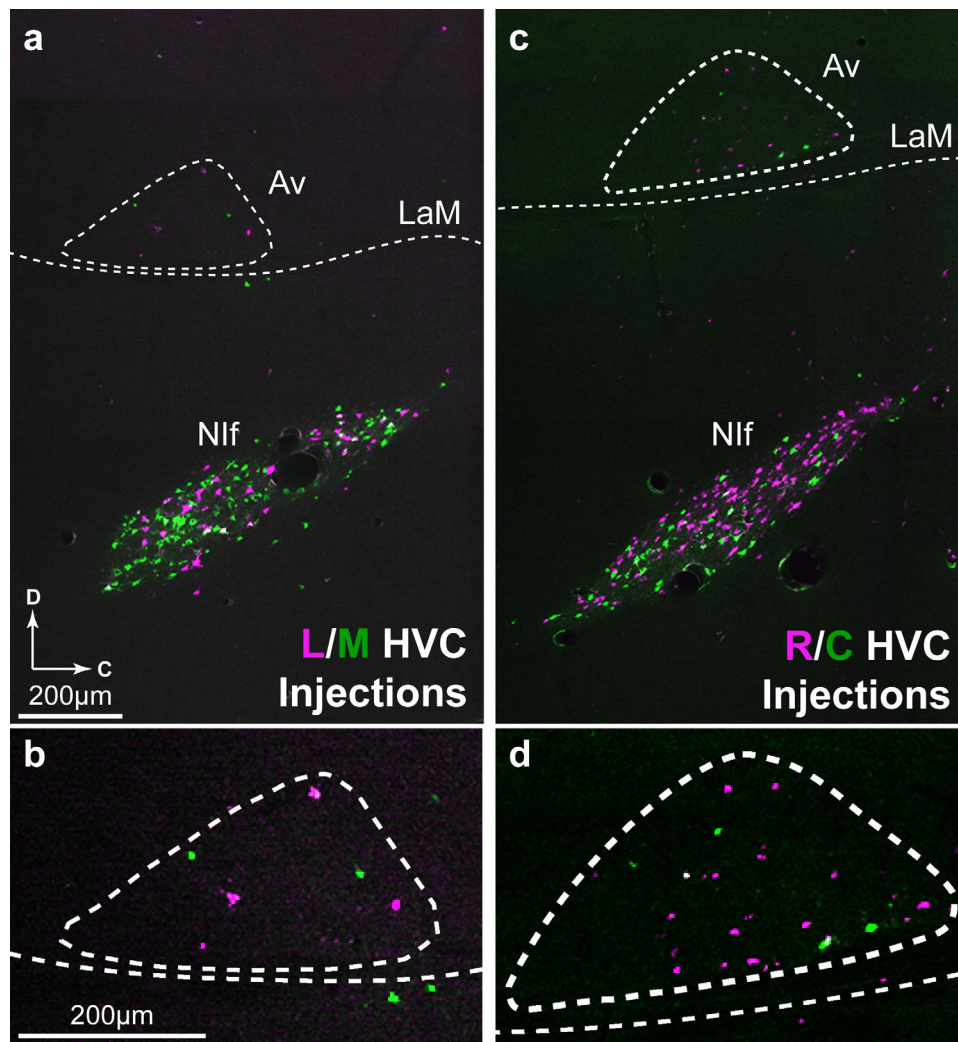
FIGURE 8 Av cells target different HVC loci in parallel. Sagittal tissue sections show that injection site pairs targeted to lateral and medial HVC (a, b) or rostral and caudal HVC (c, d) produce single-labeled subpopulations of Av neurons. Av (outlined in white) sits immediately dorsal to the LaM (outlined in white). NIf is shown in (a) and (b) for reference; the position of NIf was used to identify the location of Av as in Akutagawa and Konishi (2010). The sagittal tissue section in (a, b) is from a bird where lateral (DiI, magenta) and medial (DiO, green) HVC injection sites were separated by 500 μm—the single-labeling of Av neurons matches that seen in MMAN, NIf, RA, and Uva of this same bird. The sagittal tissue section in (c, d) is from a bird where rostral (DiI, magenta) and caudal (DiO, green) HVC injection sites were separated by 600 μm—the single-labeling of Av neurons matches that seen in MMAN, NIf, RA, and Uva of this same bird. Note that the inverse rostral-caudal topography of NIf input to HVC (see Figure 5d) can be observed in (c), where caudal NIf contains a greater density of magenta cells and rostral NIf contains a greater density of green cells

While a limitation of the present study is that we do not provide anterograde labeling of the axon terminals of MMAN, NIf, Uva, Av, or RA neurons, note that cells targeting different HVC loci directly neighbor one another and are intermixed throughout each nucleus (Figures 4–6, and 7). This means that injections of an anterograde tracer at any location within these nuclei will produce terminal labeling throughout the volume of HVC (as observed previously by Akutagawa & Konishi, 2010; Fortune & Margoliash, 1995; Foster & Bottjer, 1998). Our approach to this difficulty was to systematically vary the distance between focal HVC injection site pairs and then plot the percentage of double-labeled cells in MMAN, NIf, and Uva as a function of this distance (Figure 3). We did not complete this analysis for Av and RA due to the small number of retrogradely-labeled cells in these regions

(a consequence of our focal tracer injections). However, for MMAN, NIf, and Uva, squaring the distance at which cells became predominantly single labeled (400–500 μm) produces a conservative estimate of the dorsal area occupied by individual MMAN, NIf, or Uva axon terminals within HVC (0.16–0.25 mm^2). Future experiments with anterograde fills and reconstructions of only one or a few MMAN, NIf, or Uva neurons will be necessary to obtain more precise estimates of the dimensions of afferent axon terminals in HVC.

4.1 | Summary of HVC parallel connectivity

Figure 10 integrates our past (Basista et al., 2014) and present findings to summarize the parallel connectivity of HVC. Cells are filled with
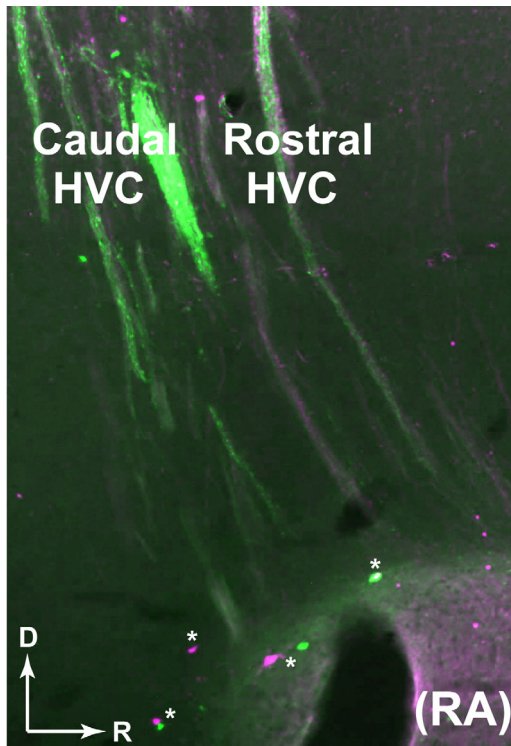
FIGURE 9 Bidirectional parallel connectivity across the rostral-caudal axis of HVC and RA. A sagittal tissue section shows that tracer injections in rostral (DiI, magenta) and caudal (DiO, green) HVC anterogradely label the axons of HVC neurons that project to RA, and retrogradely label the cells bodies of RA neurons that are reciprocally connected to HVC (asterisks). Here, rostral-caudal injection sites were separated by 420 μm and produced single-labeling of HVC axon fascicles and cell bodies in RA, similar to that seen in MMAN, NIf, Av, and Uva of this same bird. Moreover, axonal projections from rostral and caudal HVC remain distinct until reaching RA, where they both arborize throughout the volume of RA. The parallel pattern of labeling shown here following rostral-caudal HVC injection site pairs is identical to that observed previously with medial-lateral HVC injection site pairs (Basista et al., 2014)

different colors that represent different locations across the long lateral-medial axis of HVC (red, orange, green, blue, respectively) while cell outline colors represent different locations across the short rostral-caudal axis of HVC (black and white, respectively). Within HVC, neurons interconnect in a series of parallel rostral-caudal swaths (one swath enclosed by a dashed line) that have limited anatomical or functional connectivity across the lateral-medial axis of HVC (Poole et al., 2012; Stauffer et al., 2012). Although not depicted here, each swath includes all three HVC cell types (HVC-RA projection neurons, HVC-Area X projection neurons, interneurons), which are interconnected and arranged in a mosaic (Kosche et al., 2015; Mooney & Prather, 2005; Wild et al., 2005).

The three HVC afferent nuclei shown in Figure 10 (MMAN, NIf, Uva) each contain a mixture of different neuronal subpopulations that target different HVC loci in parallel. However, differences in the distribution of fill and line colors show that MMAN, NIf, and Uva each

provide a unique pattern of afferent input to HVC. For example, MMAN cells target HVC in a population-level topography across the lateral-medial (Figure 4c,g) but not the rostral-caudal (Figure 4d,h) axis. In contrast, NIf cells show no evidence of organization across the lateral-medial axis (Figure 6c,g and see NIf in Figure 8a). Instead, they project to HVC with an inverted population-level topography across the rostral-caudal axis—caudal NIf cells primarily target rostral HVC, and rostral NIf cells primarily target caudal HVC (Figure 6d,h and see NIf in Figure 8c). While population-level topography was not detected in Uva (Figure 7), more Uva cells target the lateral portion of HVC than the medial portion (Basista et al., 2014, present results). A series of parallel efferent axon bundles then exit HVC toward RA, terminating in an overlapping fashion within RA. It is the HVC-RA neurons that drive production of the learned song pattern through RA (reviewed in Bertram, Daou, Hyson, Johnson, & Wu, 2014).

As mentioned above, the labeled populations of Av and RA cells that target HVC were too small to measure stable differences in
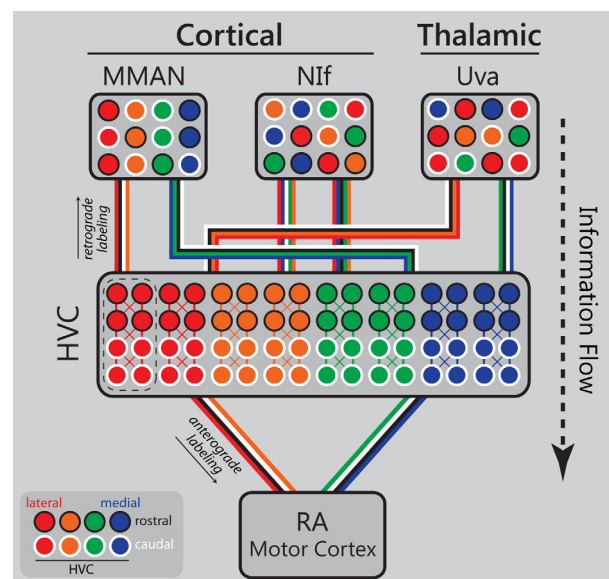

FIGURE 10 Orthogonal topography in the parallel input architecture of HVC. The parallel input architecture of HVC, which includes orthogonal topography for inputs from MMAN and NIf, suggests that HVC neural activity may be influenced by spatially-organized patterns of afferent input during the production (and possibly learning) of song. Cells in MMAN, NIf, and Uva (retrograde labeling) are filled with different colors that represent different locations across the long lateral-medial axis of HVC (red, orange, green, blue). Cell outline colors represent different locations across the short rostral-caudal axis of HVC (black and while, respectively). Note that MMAN input to HVC shows a lateral-medial topography (red, orange, green, and blue cell fills), while NIf input to HVC shows an inverse rostral-caudal topography (black and while cell outlines). Uva sends a preponderance of its input to lateral HVC (red and orange cell fills). Within HVC, neurons interconnect in a series of parallel rostral-caudal swaths (one swath enclosed by a dashed line) that have limited connectivity across the lateral-medial axis (Poole et al., 2012; Stauffer et al., 2012). A series of parallel efferent axon bundles exit HVC towards RA (anterograde labeling) to drive production of the learned song pattern. See text for additional details

topography and so are not included in Figure 10. Similarly, the projection from HVC to Area X is not included in Figure 10—the axons of HVC-X neurons are not fasciculated like those of HVC-RA neurons (Figure 9) and the focal HVC injection site pairs did not produce discernable differences in the labeling of HVC-X axons or axon terminals in Area X. Larger HVC injection site pairs may be necessary to test the predicted lateral-medial topography in HVC connectivity to Area X (Jarvis et al., 1998; Kubikova, Turner, & Jarvis, 2007).

Although avian cortical regions lack the distinctive Nissl-defined laminar and columnar organization characteristic of most regions of mammal cortex, hodological analysis is leading to a new assessment of avian/mammal homologies at the level of neural connectivity (Faunes, Francisco Botelho, Ahumada Galleguillos, & Mpodozis, 2015; Karten, 2015). In this regard, the circuitry shown in Figure 10 may begin to bring the connectivity of avian vocal-motor networks into line with the connectivity of primate motor-cortical networks (which were detected using similar retrograde tracing methods—Dea, Hamadjida, Elgbeili, Quessy, & Dancause, 2016; Hamadjida, Dea, Deffeyes, Quessy, & Dancause, 2016; Stepniewska, Preuss, & Kaas, 2006). That is, the expanded behavioral repertoire of primates—particularly the hands and digits—is associated with modular and highly parallel patterns of sensorimotor connectivity that transit distinct subregions of premotor and motor cortex, including parallel closed-loop circuitry between premotor and motor cortex (Dea et al., 2016; Hamadjida et al., 2016). The present data suggest that the expanded vocal repertoire of songbirds is associated with similar patterns of premotor and motor connectivity—HVC neurons are organized by connectivity into a number of modular cell groups, patterns of convergent sensorimotor input transit each module in a highly parallel fashion (Figure 10), and a parallel closed-loop circuit connects premotor (HVC) and motor (RA) cortex (Figure 9). Thus, despite well-known differences in the Nissl-stained appearance of cortical tissue in birds and mammals, the vertebrate brain may rely on similar patterns of neural connectivity to adjust to expansion in behavioral repertoire.

4.2 | Implications for the encoding and learning of song

The parallel architecture depicted in Figure 10 suggests that the motor production of song is ultimately encoded in a piecemeal fashion, where the individual elements of song (e.g., individual syllables, transitions from one syllable to the next, or the silent gaps between syllables) are encoded by parallel streams of neural activity that transit HVC and integrate at RA. Parallel, piecemeal encoding is supported by observations that juvenile birds show piecemeal learning of their songs. That is, individual syllables or syllable transitions can be learned independently of one another and new song elements can be learned and added to the song sequence without affecting already-learned and encoded elements (Lipkind et al., 2013; Ravbar, Lipkind, Parra, & Tchernichovski, 2012; Vallentin, Kosche, Lipkind, & Long, 2016). This remarkable flexibility could be supported by the parallel HVC architecture that we describe—learning-related activity at one HVC location need not interfere with activity in another. Further support for a parallel model of song encoding comes from evidence that medial and lateral portions of

HVC play distinct, independent roles in the production of the learned adult song (Basista et al., 2014; Poole et al., 2012).

The parallel architecture of HVC also suggests the possibility of parallel control of the muscles of respiration and vocalization. RA projection neurons are organized myotopically with respect to these muscles. Distinct subpopulations of projection neurons in dorsal, intermediate, and ventral RA influence respiration, the ventral vocal muscles, and the dorsal vocal muscles, respectively (Vicario, 1991). While anterograde labeling from our focal HVC tracer injections consistently filled the volume of RA with terminal labeling, mapping the terminal arbors of individual HVC-RA neurons suggests that each neuron is selectively targeted to one of the three RA subpopulations (Yip et al., 2012). If so, one possibility is that each labeled bundle of HVC efferent axons (Figure 9) maps broadly onto the overall RA myotopy, with each bundle containing the terminal connectivity necessary to coordinate both respiration and vocalization. Alternatively, each bundle of efferent axons could vary in terminal connectivity in RA, perhaps via differential patterns of contact with RA projection neurons and interneurons, so that each bundle controls only a portion of the overall myotopy. In this scenario, the orthogonal input topography of MMAN and NIf could potentially form a mapping of the overall RA myotopy within HVC.

We do not know whether the striking orthogonal topography of MMAN and NIf input to HVC is established before or during juvenile song learning. However, developmental and auditory-dependent refinement of topographic connectivity has been observed elsewhere in the forebrain network that controls song (Iyengar & Bottjer, 2002; Iyengar, Viswanathan, & Bottjer, 1999; Johnson, Sablan, & Bottjer, 1995; Miller-Sims & Bottjer, 2012). We do know that both MMAN and NIf are necessary for juvenile song learning (Foster & Bottjer, 2001; Naie & Hahnloser, 2011; Piristine et al., 2016) and that both are active during the motor act of singing (Kubikova et al., 2007; Lewandowski & Schmidt, 2011; Matheson, Sun, & Sakata, 2016; Vyssotski, Stepien, Keller, & Hahnloser, 2016). Although the sensory and/or motor dimensions that might be encoded across either topography (MMAN or NIf) are presently unknown, one intriguing possibility is that the orthogonal topography of MMAN and NIf input could serve as a mechanism for learning-related coincidence detection, one capable of selectively targeting any HVC location. In support of this possibility, HVC neurons express NMDA receptors (Wada, Sakaguchi, Jarvis, & Hagiwara, 2004) and antagonism of HVC NMDA receptors interferes with song learning by juveniles (Roberts et al., 2012). Evidence that organized rostral-caudal neural activity is a feature of adult, but not juvenile, HVC (Day et al., 2013) further suggests a possible relationship between the rostral-caudal organization of NIf input, the development of organized rostral-caudal neural activity within HVC, and juvenile song learning.

Figure 10 also depicts our finding that input from the thalamic nucleus Uva preferentially targets lateral HVC. Uva receives polymodal sensory input (Coleman, Roy, Wild, & Mooney, 2007; Wild, 1994; Wild & Gaede, 2016). In turn, Uva's ascending sensory input to HVC appears to drive and/or modulate production of the adult song—bilateral ablation of Uva abolishes the structure of the learned adult song (Coleman & Vu, 2005; Williams & Vicario, 1993) and cooling of Uva alters the

temporal organization of song (Hamaguchi, Tanaka, & Mooney, 2016). Thus, the polymodal sensory information relayed by Uva, along with preferential targeting of lateral HVC, may explain why the stimulus properties of female conspecifics elicit male singing, and why this female-directed singing produces a lateral-medial difference in immediate-early gene expression across HVC (Jarvis et al., 1998). The lateral-medial difference in Uva input to HVC may also inform the functional independence of lateral and medial HVC in the production of the learned adult song (Basista et al., 2014; Poole et al., 2012).

4.3 | Implications for computational models of song encoding

Several computational models of HVC song encoding have envisioned a serial feedforward chain of neurons that encodes the entire syllable sequence in millisecond increments (Bertram et al., 2014; Drew & Abbott, 2003; Fee, Kozhevnikov, & Hahnloser, 2004; Jin, Ramazanoğlu, & Seung, 2007; Li & Greenside, 2006; Long et al.,2010; Otchy et al., 2015; Weber & Hahnloser, 2007). Such models are supported by evidence that individual HVC-RA neurons generate only one or two bursts of activity at specific temporal loci during production of the syllable sequence (Hahnloser et al., 2002; Lynch et al., 2016; Picardo et al., 2016). In theory, linking many sparse-bursting HVC-RA neurons in a feedforward chain could generate the precise temporal structure of song. Indeed, the results of HVC cooling and heating experiments are consistent with this view (Long & Fee, 2008). However, as mentioned above, the parallel HVC anatomy described here appears to favor piece-meal encoding of the syllable sequence, where the individual elements of song are encoded by a number of individual input/output pathways that traverse HVC in parallel. While the timing of the individual elements of song could still be encoded by individual feedforward chains of HVC neurons, encoding of the entire syllable sequence by a single feedforward chain seems unlikely. Instead, models that focus on the individual gestural elements of song (Amador et al., 2013), or models incorporating multiple parallel recurrent loops that link the vocal-motor brainstem, Uva, and HVC (Alonso, Trevisan, Amador, Goller, & Mindlin, 2015; Gibb, Gentner, & Abarbanel, 2009; Hamaguchi et al., 2016), would seem to be more compatible with our observations. A key question for future research will be to map the input architecture of Uva, and to determine whether the parallel architecture that we have described extends to the ascending afferent pathways that drive activity in Uva.

AUTHOR CONTRIBUTIONS

KCE conducted all experimental work and collection of anatomical tract tracing data. KCE was assisted by Derrick Shaughnessy, Erin Wall, Donald Debevoise, Alan Suero, Tatum Carr, and Fred Snyder. All authors contributed to data analysis and manuscript preparation.

REFERENCES

Akutagawa, E., & Konishi, M. (2010). New brain pathways found in the vocal control system of a songbird. *Journal of Comparative Neurology*, *518*, 3086–3100.

Alonso, R. G., Trevisan, M. A., Amador, A., Goller, F., & Mindlin, G. B. (2015). A circular model for song motor control in Serinus canaria. *Frontiers in Computational Neuroscience*, *9*, 41.

Amador, A., Perl, Y. S., Mindlin, G. B., & Margoliash, D. (2013). Elemental gesture dynamics are encoded by song premotor cortical neurons. *Nature*, *495*, 59–64.

Andalman, A. S., Foerster, J. N., & Fee, M. S. (2011). Control of vocal and respiratory patterns in birdsong: Dissection of forebrain and brainstem mechanisms using temperature. *PLoS One*, *6*, e25461

Aronov, D., Andalman, A. S., & Fee, M. S. (2008). A specialized forebrain circuit for vocal babbling in the juvenile songbird. *Science*, *320*, 630–634.

Aronov, D., Veit, L., Goldberg, J. H., & Fee, M. S. (2011). Two distinct modes of forebrain circuit dynamics underlie temporal patterning in the vocalizations of young songbirds. *The Journal of Neuroscience*, *31*, 16353–16368.

Basista, M. J., Elliott, K. C., Wu, W., Hyson, R. L., Bertram, R., & Johnson, F. (2014). Independent premotor encoding of the sequence and structure of birdsong in avian cortex. *The Journal of Neuroscience*, *34*, 16821–16834.

Bauer, E. E., Coleman, M. J., Roberts, T. F., Roy, A., Prather, J. F., & Mooney, R. (2008). A synaptic basis for auditory-vocal integration in the songbird. *The Journal of Neuroscience*, *28*, 1509–1522.

Bertram, R., Daou, A., Hyson, R. L., Johnson, F., & Wu, W. (2014). Two neural streams, one voice: Pathways for theme and variation in the songbird brain. *Neuroscience*, *277*, 806–817.

Bottjer, S. W., Halsema, K. A., Brown, S. A., & Miesner, E. A. (1989). Axonal connections of a forebrain nucleus involved with vocal learning in zebra finches. *Journal of Comparative Neurology*, *279*, 312–326.

Coleman, M. J., & Vu, E. T. (2005). Recovery of impaired songs following unilateral but not bilateral lesions of nucleus uvaeformis of adult zebra finches. *Journal of Neurobiology*, *63*, 70–89.

Coleman, M. J., Roy, A., Wild, J. M., Mooney, R. (2007). Thalamic gating of auditory responses in telencephalic song control nuclei. *The Journal of Neuroscience*, *27*, 10024–10036.

Day, N. F., Terleski, K. L., Nykamp, D. Q., & Nick, T. A. (2013). Directed functional connectivity matures with motor learning in a cortical pattern generator. *Journal of Neurophysiology*, *109*, 913–923.

Dea, M., Hamadjida, A., Elgbeili, G., Quessy, S., & Dancause, N. (2016). Different patterns of cortical inputs to subregions of the primary motor cortex hand representation in Cebus apella. *Cerebral Cortex 26*, 1747-1761.

Drew, P. J., & Abbott, L. F. (2003). Model of song selectivity and sequence generation in area HVc of the songbird. *Journal of Neurophysiology*, *89*, 2697–2706.

Faunes, M., Francisco Botelho, J., Ahumada Galleguillos, P., & Mpodozis, J. (2015). On the hodological criterion for homology. *Frontiers in Neuroscience*, *9*, 223.

Fee, M. S., Kozhevnikov, A. A., & Hahnloser, R. H. (2004). Neural mechanisms of vocal sequence generation in the songbird. *Annals of the New York Academy of Sciences*, *1016*, 153–70.

Fortune, E. S., & Margoliash, D. (1995). Parallel pathways and convergence onto HVc and adjacent neostriatum of adult zebra finches (Taeniopygia guttata). *Journal of Comparative Neurology*, *360*, 413–441.

Foster, E. F., & Bottjer, S. W. (1998). Axonal connections of the high vocal center and surrounding cortical regions in juvenile and adult male zebra finches. *Journal of Comparative Neurology*, *397*, 118–138.

Foster, E. F., & Bottjer, S. W. (2001). Lesions of a telencephalic nucleus in male zebra finches: Influences on vocal behavior in juveniles and adults. *Journal of Neurobiology*, *46*, 142–165.

Gibb, L., Gentner, T. Q., & Abarbanel, H. D. (2009). Brain stem feedback in a computational model of birdsong sequencing. *Journal of Neurophysiology*, *102*, 1763–178.

Hahnloser, R. H., Kozhevnikov, A. A., & Fee, M. S. (2002). An ultrasparse code underlies the generation of neural sequences in a songbird. *Nature*, *419*, 65–70.

Hamadjida, A., Dea, M., Deffeyes, J., Quessy, S., & Dancause, N. (2016). Parallel cortical networks formed by modular organization of primary motor cortex outputs. *Current Biology*, *26*, 1737–1743.

Hamaguchi, K., & Mooney, R. (2012). Recurrent interactions between the input and output of a songbird cortico-basal ganglia pathway are implicated in vocal sequence variability. *The Journal of Neuroscience*, *32*, 11671–11687.

Hamaguchi, K., Tanaka, M., & Mooney, R. (2016). A distributed recurrent network contributes to temporally precise vocalizations. *Neuron*, *91*, 680–693.

Hamaguchi, K., Tschida, K. A., Yoon, I., Donald, B. R., & Mooney, R. (2014). Auditory synapses to song premotor neurons are gated off during vocalization in zebra finches. *Elife*, *3*, e01833.

Iyengar, S., & Bottjer, S. W. (2002). The role of auditory experience in the formation of neural circuits underlying vocal learning in zebra finches. *The Journal of Neuroscience*, *22*, 946–958.

Iyengar, S., Viswanathan, S. S., & Bottjer, S. W. (1999). Development of topography within song control circuitry of zebra finches during the sensitive period for song learning. *The Journal of Neuroscience*, *19*, 6037–6057.

Jarvis, E. D., & Nottebohm, F. (1997). Motor-driven gene expression. *Proceedings of the National Academy of Sciences of the United States of America*, *94*, 4097–4102.

Jarvis, E. D., Scharff, C., Grossman, M. R., Ramos, J. A., & Nottebohm, F. (1998). For whom the bird sings: Context-dependent gene expression. *Neuron*, *21*, 775–788.

Johnson, F., Sablan, M. M., & Bottjer, S. W. (1995). Topographic organization of a forebrain pathway involved with vocal learning in zebra finches. *Journal of Comparative Neurology*, *358*, 260–278.

Jin, D. Z., Ramazanoğlu, F. M., & Seung, H. S. (2007). Intrinsic bursting enhances the robustness of a neural network model of sequence generation by avian brain area HVC. *Journal of Computational Neuroscience*, *23*, 283–299.

Jin, H., & Clayton, D. F. (1997). Localized changes in immediate-early gene regulation during sensory and motor learning in zebra finches. *Neuron*, *19*, 1049–1059.

Karten, H. J. (2015). Vertebrate brains and evolutionary connectomics: On the origins of the mammalian 'neocortex'. *Philosophical Transactions of the Royal Society of London Series B, Biological Sciences*, *370*, 20150060.

Kosche, G., Vallentin, D., & Long, M. A. (2015). Interplay of inhibition and excitation shapes a premotor neural sequence. *The Journal of Neuroscience*, *35*, 1217–1227.

Kozhevnikov, A. A., & Fee, M. S. (2007). Singing-related activity of identified HVC neurons in the zebra finch. *Journal of Neurophysiology*, *97*, 4271–4283.

Kubikova, L., Turner, E. A., & Jarvis, E. D. (2007). The pallial basal ganglia pathway modulates the behaviorally driven gene expression of the motor pathway. *European Journal of Neuroscience*, *25*, 2145–2160.

Lewandowski, B. C., & Schmidt, M. (2011). Short bouts of vocalization induce long-lasting fast γ oscillations in a sensorimotor nucleus. *The Journal of Neuroscience*, *31*, 13936–13948.

Li, M., & Greenside, H. (2006). Stable propagation of a burst through a one-dimensional homogeneous excitatory chain model of songbird nucleus HVC. *Physical Review E Statistical, Nonlinear, and Soft Matter Physics*, *74*, 011918.

Lipkind, D., Marcus, G. F., Bemis, D. K., Sasahara, K., Jacoby, N., Takahasi, M., . . . Tchernichovski, O. (2013). Stepwise acquisition of vocal combinatorial capacity in songbirds and human infants. *Nature*, *498*, 104–108.

Long, M. A., & Fee, M. S. (2008). Using temperature to analyze temporal dynamics in the songbird motor pathway. *Nature*, *456*, 189–194.

Long, M. A., Jin, D. Z., & Fee, M. S. (2010). Support for a synaptic chain model of neuronal sequence generation. *Nature*, *468*, 394–399.

Lynch, G. F., Okubo, T. S., Hanuschkin, A., Hahnloser, R. H., & Fee, M. S. (2016). Rhythmic continuous-time coding in the songbird analog of vocal motor cortex. *Neuron*, *90*, 877–892.

Markowitz, J. E., Liberti, W. A., 3rd, Guitchounts, G., Velho, T., Lois, C., & Gardner, T. J. (2015). Mesoscopic patterns of neural activity support songbird cortical sequences. *PLoS Biology*, *13*, e1002158.

Matheson, L. E., Sun, H., & Sakata, J. T. (2016). Forebrain circuits underlying the social modulation of vocal communication signals. *Developmental Neurobiology*, *76*, 47–63.

Miller-Sims, V. C., & Bottjer, S. W. (2012). Auditory experience refines cortico-basal ganglia inputs to motor cortex via remapping of single axons during vocal learning in zebra finches. *Journal of Neurophysiology*, *107*, 1142–1156.

Mooney, R., & Prather, J. F. (2005). The HVC microcircuit: The synaptic basis for interactions between song motor and vocal plasticity pathways. *The Journal of Neuroscience*, *25*, 1952–1964.

Naie, K., & Hahnloser, R. H. (2011). Regulation of learned vocal behavior by an auditory motor cortical nucleus in juvenile zebra finches. *Journal of Neurophysiology*, *106*, 291–300.

Nottebohm, F., Kelley, D. B., & Paton, J. A. (1982). Connections of vocal control nuclei in the canary telencephalon. *Journal of Comparative Neurology*, *207*, 344–357.

Nottebohm, F., Stokes, T. M., & Leonard, C. M. (1976). Central control of song in the canary, Serinus canarius. *Journal of Comparative Neurology*, *165*, 457–486.

Okubo, T. S., Mackevicius, E. L., Payne, H. L., Lynch, G. F., & Fee, M. S. (2015). Growth and splitting of neural sequences in songbird vocal development. *Nature*, *528*, 352–357.

Otchy, T. M., Wolff, S. B., Rhee, J. Y., Pehlevan, C., Kawai, R., Kempf, A., . . . Ölveczky, B. P. (2015). Acute off-target effects of neural circuit manipulations. *Nature*, *528*, 358–363.

Picardo, M. A., Merel, J., Katlowitz, K. A., Vallentin, D., Okobi, D. E., Benezra, S. E., . . . Long, M. A. (2016). Population-level representation of a temporal sequence underlying song production in the zebra finch. *Neuron*, *90*, 866–876.

Piristine, H. C., Choetso, T., & Gobes, S. M. (2016). A sensorimotor area in the songbird brain is required for production of vocalizations in the song learning period of development. *Developmental Neurobiology*, doi: 10.1002/dneu.22384.

Poole, B., Markowitz, J. E., & Gardner, T. J. (2012). The song must go on: Resilience of the songbird vocal motor pathway. *Plos One*, 7, e38173.

Ravbar, P., Lipkind, D., Parra, L. C., & Tchernichovski, O. (2012). Vocal exploration is locally regulated during song learning. *The Journal of Neuroscience*, 32, 3422–3432.

Roberts, T. F., Gobes, S. M., Murugan, M., Ölveczky, B. P., & Mooney, R. (2012). Motor circuits are required to encode a sensory model for imitative learning. *Nature Neuroscience*, 15, 1454–1459.

Roberts, T. F., Klein, M. E., Kubke, M. F., Wild, J. M., & Mooney, R. (2008). Telencephalic neurons monosynaptically link brainstem and forebrain premotor networks necessary for song. *The Journal of Neuroscience*, 28, 3479–3489.

Scharff, C., Kirn, J. R., Grossman, M., Macklis, J. D., & Nottebohm, F. (2000). Targeted neuronal death affects neuronal replacement and vocal behavior in adult songbirds. *Neuron*, 25, 481–492.

Simpson, H. B., & Vicario, D. S. (1990). Brain pathways for learned and unlearned vocalizations differ in zebra finches. *The Journal of Neuroscience*, 10, 1541–1556.

Stauffer, T. R., Elliott, K. C., Ross, M. T., Basista, M. J., Hyson, R. L., & Johnson, F. (2012). Axial organization of a brain region that sequences a learned pattern of behavior. *The Journal of Neuroscience*, 32, 9312–9322.

Stepniewska, I., Preuss, T. M., & Kaas, J. H. (2006). Ipsilateral cortical connections of dorsal and ventral premotor areas in New World owl monkeys. *Journal of Comparative Neurology*, 495, 691–708.

Thompson, J. A., & Johnson, F. (2007). HVC microlesions do not destabilize the vocal patterns of adult male zebra finches with prior ablation of LMAN. *Developmental Neurobiology*, 67, 205–218.

Thompson, J. A., Wu, W., Bertram, R., & Johnson, F. (2007). Auditory-dependent vocal recovery in adult male zebra finches is facilitated by lesion of a forebrain pathway that includes the basal ganglia. *The Journal of Neuroscience*, 27, 12308–12320.

Vallentin, D., Kosche, G., Lipkind, D., & Long, M. A. (2016). Neural circuits. Inhibition protects acquired song segments during vocal learning in zebra finches. *Science*, 351, 267–271.

Vallentin, D., & Long, M. A. (2015). Motor origin of precise synaptic inputs onto forebrain neurons driving a skilled behavior. *The Journal of Neuroscience*, 35, 299–307.

Vu, E. T., Mazurek, M. E., & Kuo, Y. C. (1994). Identification of a forebrain motor programming network for the learned song of zebra finches. *The Journal of Neuroscience*, 14, 6924–6934.

Vyssotski, A. L., Stepien, A. E., Keller, G. B., & Hahnloser, R. H. (2016). A neural code that is isometric to vocal output and correlates with its sensory consequences. *PLoS Biology*, 14, e2000317.

Wada, K., Sakaguchi, H., Jarvis, E. D., & Hagiwara, M. (2004). Differential expression of glutamate receptors in avian neural pathways for learned vocalization. *Journal of Comparative Neurology*, 476, 44–64.

Weber, A. P., & Hahnloser, R. H. (2007). Spike correlations in a songbird agree with a simple Markov population model. *PLoS Computational Biology*, 3, e249.

Wild, J. M. (1994). Visual and somatosensory inputs to the avian song system via nucleus uvaeformis (Uva) and a comparison with the projections of a similar thalamic nucleus in a nonsongbird, Columba livia. *Journal of Comparative Neurology*, 349, 512–535.

Wild, J. M., & Gaede, A. H. (2016). Second tectofugal pathway in a songbird (Taeniopygia guttata) revisited: Tectal and lateral pontine projections to the posterior thalamus, thence to the intermediate nidopallium. *Journal of Comparative Neurology*, 524, 963–985.

Wild, J. M., Williams, M. N., Howie, G. J., & Mooney, R. (2005). Calcium-binding proteins define interneurons in HVC of the zebra finch (Taeniopygia guttata). *Journal of Comparative Neurology*, 483, 76–90.

Williams, H., Crane, L. A., Hale, T. K., Esposito, M. A., & Nottebohm, F. (1992). Right-side dominance for song control in the zebra finch. *Journal of Neurobiology*, 23, 1006–1020.

Williams, H., & Vicario, D. S. (1993). Temporal patterning of song production: Participation of nucleus uvaeformis of the thalamus. *Journal of Neurobiology*, 24, 903–912.

Yu, A. C., & Margoliash, D. (1996). Temporal hierarchical control of singing in birds. *Science*, 273, 1871–1875.